universität wien

MASTERARBEIT | MASTER'S THESIS

Titel | Title

Setup optimization and improvement of the data analysis for the electro-optic fluorescence lifetime imaging microscopy (EOFLIM) project

verfasst von | submitted by

Daniel Aziz BSc

angestrebter akademischer Grad | in partial fulfilment of the requirements for the degree of

Master of Science (MSc)

Wien | Vienna, 2024

Studienkennzahl lt. Studienblatt | Degree programme code as it appears on the student record sheet:	UA 066 876
Studienrichtung lt. Studienblatt | Degree programme as it appears on the student record sheet:	Masterstudium Physics
Betreut von | Supervisor:	Assoz. Prof. Dipl.-Ing. Dr. Thomas Juffmann

Acknowledgements

First of all, I want to thank Thomas Juffmann for giving me the opportunity to work on this amazing project and for always finding time to discuss the next steps with us. Secondly, Raphaël Marchand deserves a big thank you for many, many fruitful discussions and for guiding me through the time in this group. Next, I want to thank Franz I. Pfanner for giving me the resources to learn Python. Programming truly is the Wild, Wild West in Physics, just as you said. Nele Jarnot and Victoria Helm - thanks for the fun times in the lab! For initially sparking my interest in Physics, I want to thank my high-school teacher Gregor Slavik. Without you, I would be a chemist now. Lastly, I want to thank my friends, my family and my dog, Macho, for cheering me up all the time and allowing my brain to shut off.
Thank you!

Abstract

Fluorescence lifetime imaging microscopy (FLIM) is a technique used in the realm of biomedical imaging and can, through the properties of fluorescence lifetime, act as an indicator for changes in pH, viscosity, or chemical concentration. Images are taken in one of two acquisition modes: Confocal laser scanning or wide-field microscopy. While scanning produces images with better resolution, it is very slow compared to wide-field microscopy.
The EOFLIM setup is a FLIM microscope utilizing an electro-optic (EO) element to time-bin incoming fluorescence signals, thus combining the speed of wide-field FLIM and the sensitivity of scanning FLIM. The goal of this thesis is to prepare the setup for two upcoming collaborations. The first, a collaboration with the Huser Group of the University of Bielefeld (UNIBIE), will feature the EOFLIM setup as a module of their Structured Illumination Microscope (SIM) to capture super-resolution FLIM images of cells and tissues. With the Unterhuber Group of the Medical University of Vienna (MEDUVIE), the second collaboration will compare the EOFLIM to the FLIM setups the collaborators already use in the domain of brain-tumor surgery regarding noise, photon collection efficiency, and frame rate.
To prepare the setup, experimental and computational work, as well as simulations have to be done. This includes reducing aberrations by evaluating optical elements with a wavefront sensor, simulating point-spread functions of current optical elements and potential acquisitions. The data analysis is refined to sub-pixel accuracy by modifying or creating Matlab and Python scripts that fulfill the needs of the setup and scientists. Experimental and simulation analysis led to buying new optical elements, which improved the quality and fidelity of the optical system. The computational tasks increased the accuracy, speed, and ease of use of the data analysis.

Kurzfassung

Fluoreszenzlebensdauer-Mikroskopie (eng.: FLIM) ist eine Technik, die im Rahmen von biomedizinischer Bildgebung eingesetzt wird und kann, durch die Eigenschaften der Fluoreszenzlebensdauer, als Indikator für Änderungen des pH-Wertes, der Viskosität oder chemischen Konzentration fungieren. Bilder werden in einer von zwei Erfassungsmodi aufgenommen: Raster-FLIM oder Weitfeld-FLIM. Während Raster-FLIM Bilder in höherer Auflösung produziert, ist es sehr langsam im Vergleich zu Weitfeld-FLIM.
Der EOFLIM Aufbau ist ein FLIM Mikroskop, das ein elektro-optisches (EO) Element als temporäre Takteinheit nutzt, wodurch es die Geschwindigkeit von Weitfeld-FLIM und die Sensitivität von Raster-FLIM kombiniert. Das Ziel dieser Arbeit ist, den Aufbau für zwei bevorstehende Kollaborationen vorzubereiten. Die Erste, eine Kollaboration mit der Huser Group der Universität Bielefeld (UNIBIE), wird den EOFLIM Aufbau als Modul ihres Structured Illumination Microscope (SIM) nutzen, um Bilder von Zellen und Gewebe in ultrahoher Auflösung aufzunehmen. Gemeinsam mit der Unterhuber Group der Medizinischen Universität Wien (MEDUVIE) handelt die zweite Kollaboration davon, deren FLIM Aufbau mit dem EOFLIM Aufbau bezüglich deren Anwendbarkeit bei der Gehirntumorentfernung zu vergleichen. Insbesondere sollen sie Photonenausbeute, die Bildwiederholungsrate, sowie das erreichbare Signal-Rausch-Verhätlnis untersucht werden.
Um den Aufbau vorzubereiten, sind experimentelle Arbeit und Simulationen notwendig. Dies beinhaltet eine Reduktion der optischen Aberrationen durch Evaluation optischer Elemente durch einen Wellenfrontsensor und die Simulation von Punktspreizfunktionen von gegenwärtigen und potenziell zukünftigen optischen Elementen. Computerarbeit wird im Rahmen von Verfeinerung der Datenanalyse zur sub-pixel Genauigkeit durch Modifikation vorhandener oder Erstellung neuer Matlab und Python Skripte, welche die Voraussetzungen des Aufbaus und der Wissenschafter erfüllen, durchgeführt. Sowohl die experimentelle als auch die Simulationsanalyse führte zum Kauf neuer optischer Elemente, die die Qualität und Güte des optischen Systems erhöhten. Die Programmieraufgaben verbesserten Genauigkeit, Geschwindigkeit und Nutzerfreundlichkeit der Datenanalyse.

Contents

List of Tables

List of Figures

1 Introduction

Fluorescence was first observed in the middle of the 19th century by Sir Frederik William Herschel [1]. About 50 years later, the first commercial Fluorescence Microscope was available. Since then, many techniques have branched off from it and found a place in the fields of material and life sciences [2, 3]. The 2014 Nobel Prize for Chemistry was awarded to two different Fluorescence Microscopy techniques. The first one is Stimulated Emission Depletion (STED) by Stefan Hell [4] which managed to go beyond Abbe's diffraction limit. The second one was invented separately by Eric Betzig and William E. Moerner and is called Single-Molecule Microscopy [5], and is the basis for other super-resolution techniques like STORM or PALM [6].
In the 1980s a technique called Fluorescence Lifetime Imaging Microscopy (FLIM) was developed. It uses the fluorescence lifetime instead of fluorescence intensity as a signal. The fluorescence lifetime is the average time a fluorophore - a substance that can fluoresce - is in the excited state. FLIM brought advantages over the conventional fluorescence microscope: It is fluorophore concentration independent. It provides insight into a range of biomolecular interactions and intracellular processes as it is dependent on various physico- as well biochemical parameters, unlike fluorescence intensity [3]. Additionally, with FLIM, one can differentiate fluorophores which emit at the same wavelength but with different lifetimes.
Confocal laser scanning and wide-field microscopy can be used for FLIM, each with their respective advantages and drawbacks [7–10]. While confocal laser scanning techniques produce high-resolution images with good signal-to-noise ratios (SNR), they are limited by their slow acquisition speed. Wide-field microscopy on the other hand have high acquisition rates but suffer from high read noise, low quantum efficiency, or photon losses during the detector's dead time.
EOFLIM, first introduced in 2019 by scientists of the Kasevich Group at Stanford, including Thomas Juffmann, [11], tries to overcome these drawbacks by combining the sensitivity of scanning and the speed of wide-field microscopy. This is done by time-gating the incoming signal with an electro-optic modulator. The EOFLIM project aims to demonstrate the potential of this setup by utilizing it for two different collaborations. First, in the realm of super-resolution imaging, combining it with the SIM setup of the Huser Group [12] (Universität Bielefeld) to produce super-resolution lifetime images of live cells and tissues. Secondly, the EOFLIM setup will be compared to the FLIM setups present in the Unterhuber Group of the MEDUVIE (Medizinische Universität Wien), located at one of Europe's largest hospitals, the AKH (Allgemeines Krankenhaus) Wien [13–17]. This application revolves around using FLIM systems for brain tumour surgery, where strict regulations must be met and video frame rates are important for surgical guidance using real time FLIM monitoring. Here, the setups will be compared to

each other with regards to noise, photon collection efficiency and frame rate. For both collaborations, the EOFLIM setup has to be optimised. On the one hand, aberrations have to be reduced by replacing optical elements at fault and simulating the behavior of potential new optical elements. On the other hand, the data analysis has to be improved to deliver quantitative results and to provide a user-friendly interface. This master's thesis is about the preparatory work for the collaborations.

The structure of this thesis is as follows: First, in chapter 2, we provide the theoretical background needed to understand the setup and contents of this thesis. This includes an overview of the physical principles (section 2.1), the used optics (section 2.2), an introduction to fluorescence and fluorescence lifetime imaging (section 2.3) and an introduction to the experiments of our collaborators (section 2.4). Next, we explain the EOFLIM setup itself (chapter 3) in working principle (section 3.1) and workflow (section 3.2). In Chapter 4, we conduct the experimental (section 4.1) and simulation (section 4.2) tasks of this thesis and state their results in section 4.3. Chapter 5 contains the data analysis improvements and the testing of the overlapping script by calculating the offset of Gaussian centroids of overlapped samples. The test results are in section 5.4. Finally, we conclude this thesis in chapter 6 by discussing the results and by giving an outlook for the future of the project.

2 Theoretical Background

This chapter provides the necessary knowledge to understand the imaging techniques as well as the underlying physical principles and optical elements named throughout this thesis.

2.1 Physical principles

This section provides insight into some physical principles used for the EOFLIM project and in this thesis. While people have written whole chapters or even books about these topics, here it will be comprised to the level necessary to understand this thesis.

2.1.1 Fluorescence

The fluorescence process occurs when an atom in an excited state relaxes back into its ground state by emitting a photon. For that, it first has to be excited, which can be done with a laser. It is important to note that the energy of the emitted photons is lower than the ones used to excite the fluorophore. This is due to other, faster effects happening in the excited state, which puts the atom in its lowest vibrational level of the excited state before emitting the photon. This shift in energy is called Stokes shift and can be seen in Figure 2.1.

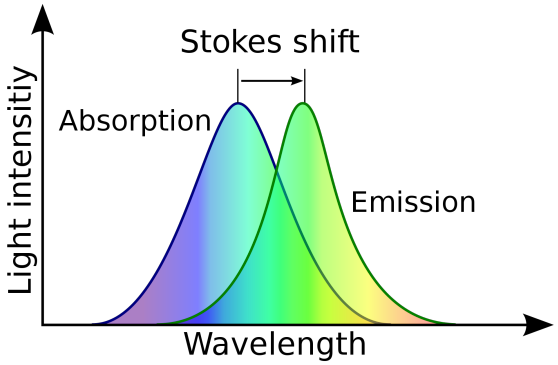

Figure 2.1: Stokes shift between absorption and emission spectrum of a fluorecent sample. As the wavelength increases, the energy decreases. Taken from [18].

Fluorescence is not guaranteed after atom excitation as there are also different non-radiative transitions an atom can take after being excited [6, 19, 20]. Figure 2.2 shows a Jablonski-Diagram with four electronic states, namely the singlet ground state S_0, the first

excited singlet state S_1, the second excited singlet state S_2, and the first excited triplet state T_1. With these states, one can show how a fluorophore may react to excitation.

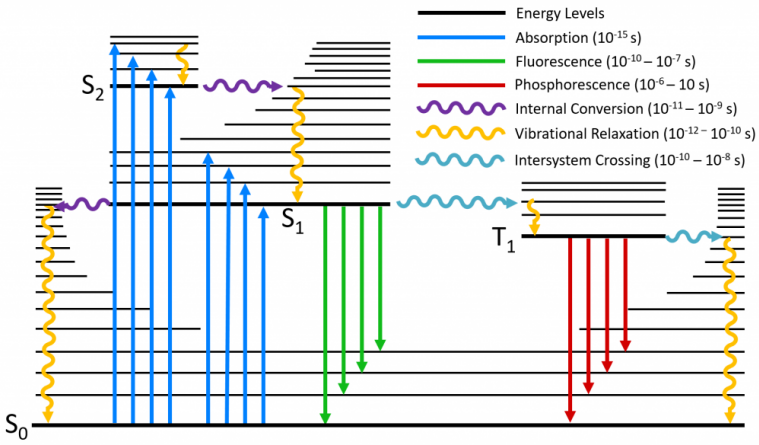

Figure 2.2: Jablonksi Diagram featuring various transitions between electronic states and their vibrational modes. Undulating arrows depict non-radiative processes. Taken from [21].

Non-radiative transitions are displayed with undulating arrows. The transitions in figure 2.2 are described in the following:

1. Absorption: Absorption is the process of converting the excitation photon energy to internal energy by elevating the atom to a higher electronic state. It is the fastest process of the Jablonski diagram with a time of about 10^{-15} s. Due to the conservation of angular momentum, the transfer from singlet ground state to triplet state is impossible. Here, it is shown by blue arrows.

2. Vibrational relaxation: The second fastest process with 10^{-12} s to 10^{-10} s is called vibrational relaxation. The yellow undulating arrows in the figure show that it is the first reaction to excitation, bringing the atom from the higher vibrational levels caused by excitation back to the lowest vibrational level within the same electronic state by transferring excess vibrational energy to the same (intramolecular) or a surrounding (intermolecular) molecule.

3. Internal Conversion: After reaching the lowest vibrational level, a reaction called Internal Conversion may happen, which transfers the energy of this electronic state to a higher vibrational mode of a lower electronic state, followed by vibrational relaxation. It is important to note that the rate of this reaction is inversely proportional to the energy gap between the two electronic states, which means that for higher electronic states, it is a rather rapid transition while it slows down between S_1 and S_0 such that it competes with other transitions. This process happens on timescales of 10^{-11} s to 10^{-9} s and is represented by a violet undulating arrow.

4. Fluorescence: As discussed before, fluorescence is a radiative process from S_1 to S_0 and the desired transition for the setup of this master thesis. This transition takes about 10^{-10} s to 10^{-7} s and is indicated by a green arrow.

5. Intersystem Crossing: Intersystem Crossing describes the transition from S_1 to T_1, which is forbidden due to spin angular momentum conservation but can be made weakly allowed by spin-orbit coupling. It is a non-radiative process with a duration of 10^{-10} s to 10^{-8} s, meaning it competes with internal conversion and fluorescence. It is depicted by undulating light-blue arrows.

6. Phosphorescence: As with intersystem crossing, this is a forbidden transition from T_1 down to S_0, which can be made weakly allowed by spin-orbit coupling. Due to the circumstances of this transition, its rate is relatively low, meaning that it takes a lot of time with timescales ranging from 10^{-6} s to 10 s. It is, like fluorescence, a radiative process, and in this figure, it is depicted by red arrows.

To stack the odds in favor of or against fluorescence one can look at specific chemical properties of the fluorophores and choose molecules which exhibit these. For example, fluorescence can be quenched by attaching a heavy molecule to the fluorophore which enhances the intersystem crossing probability. To make fluorescence more likely, one wants to use planar and rigid molecules, as these reduce the likelihood of non-radiative transitions [6].
If fluorescence did occur, the lifetime can be defined as the average duration a statistical ensemble of fluorophores spends in the excited state. A way to derive this lifetime is called TCSPC, time-correlated single-photon counting [8]. For this method, the delay between excitation pulse and photon arrival time is repeatedly measured. The arrival time of each photon is then plotted as intensity histograms (time bin in the realm of picoseconds) and results in the fluorescence decay. For a mono-exponential decay, the equation is:

$$I(t) = I_0 \ \exp(-t/\tau) \tag{2.1}$$

Where $I(t)$ is the intensity after a time t, I_0 the initial intensity and τ the lifetime of the excited state.
For multi-exponential decays, as is the case for a sample with a mixture of different lifetimes t_i, the equation changes to:

$$I(t) = \sum_i \alpha_i \ \exp(-t/\tau_i) \tag{2.2}$$

Where α_i describes the weighted contribution of each kind of fluorophore i. The mean lifetime τ_m is thus also weighted by α_i [19]:

$$\tau_m = \sum_i \alpha_i \tau_i \tag{2.3}$$

The lifetime of a fluorophore can be influenced by various physicochemical and biochemical parameters [3], for example:

1. pH: A change in pH may lead to an alteration of the molecule shape, which also changes the rate of various transitions, and thus the fluorescence lifetime [22].

2. Temperature: Higher temperatures causes higher energy states to be populated but also increase collisions (energy transfer) with surrounding molecules [23].

3. Oxygen concentration: If the oxygen concentration is very high, fluorescence may be quenched completely, called "static quenching", as the fluorophore and molecular oxygen may form a complex that prevents the fluorophore from entering the excited state. With a lower concentration, "dynamic quenching" can occur, which means that the excited fluorophore forms a short-lived complex with molecular oxygen which relaxes to the ground state by non-radiative means [24].

4. Viscosity: Non-radiative transitions are increased for rotating fluorophores. Thus, the decay rate changes with the viscosity of the solvent [25].

2.1.2 Aberrations

Ideally, every optical element works perfectly when constructing an experiment, but in reality, each introduces errors - these errors are called aberrations. They can lead to various imperfections in the resulting image, from distortions to the loss of resolution [26,27]. The most common types of aberrations are astigmatism, spherical and chromatic aberration, coma, and defocus.
To describe the propagation of light, one can use geometrical or wave optics, where light is either approximated in terms of rays or wavefronts, respectively. Wave optics can describe effects, such as interference, for which geometrical optics are not valid. To quantify how aberrated a wavefront is, one can use the so-called Zernike polynomials. Together, they form a complete orthogonal basis set on the unit circle, which allows one to decompose any wavefront and its aberrations into their Zernike components [27]. These polynomials, also called Zernike modes, have their own characteristic azimuthal and radial frequency and correspond to a specific kind of aberration. They are defined as:

$$Z_n^m(\rho,\phi) = R_n^m(\rho)\cos(m\phi) \tag{2.4}$$

for even Zernike polynomials and

$$Z_n^{-m}(\rho,\phi) = R_n^m(\rho)\sin(m\phi) \tag{2.5}$$

for odd Zernike polynomials, where even and odd mean that the function is even/odd with respect to the azimuthal angle ϕ, respectively. ρ is the radial distane with $0 \leq \rho \leq 1$, n and m are integers with $0 \leq m \leq n$. $R_n^m(\rho)$ are radial polynomials which are defined as

$$R_n^m(\rho) = \Sigma_{k=0}^{\frac{n-m}{2}} \frac{(-1)^k(n-k)!}{k!(\frac{n+m}{2}-k)!(\frac{n-m}{2}-k)!}\rho^{n-2k} \tag{2.6}$$

The Zernike modes can be indexed by their azimuthal degree n and radial order m or, by ANSI standards with a single index j which is defined by

$$j = \frac{n(n+2)+m}{2} \tag{2.7}$$

Table 2.1: The Zernike polynomials. The normalization is taken such that the peak-to-valley amplitude for each mode is unity.

Z_n^m	j	n	m	Mathematical expression	Classical name
Z_0^0	0	0	0	1	Piston
Z_1^{-1}	1	1	-1	$2\rho sin(\phi)$	Y-Tilt
Z_1^1	2	1	+1	$2\rho cos(\phi)$	X-Tilt
Z_2^{-2}	3	2	-2	$\sqrt{6}\rho^2 sin2\phi$	Oblique astigmatism
Z_2^0	4	2	0	$\sqrt{3}(2\rho^2-1)$	Defocus
Z_2^2	5	2	+2	$\sqrt{6}\rho^2 cos2\phi$	Vertical astigmatism
Z_3^{-3}	6	3	-3	$\sqrt{8}\rho^3 sin3\phi$	Vertical trefoil
Z_3^{-1}	7	3	-1	$\sqrt{8}(3\rho^3-2\rho)sin\phi$	Vertical coma
Z_3^1	8	3	+1	$\sqrt{8}(3\rho^3-2\rho)cos\phi$	Horizontal coma
Z_3^3	9	3	+3	$\sqrt{8}\rho^3 cos3\phi$	Oblique trefoil
Z_4^{-4}	10	4	-4	$\sqrt{10}\rho^4 sin4\phi$	Oblique quadrafoil
Z_4^{-2}	11	4	-2	$\sqrt{10}(4\rho^4-3\rho^2)sin2\phi$	Oblique secondary astigmatism
Z_4^0	12	4	0	$\sqrt{5}(6\rho^4-6\rho^2+1)$	Primary spherical
Z_4^2	13	4	2	$\sqrt{10}(4\rho^4-3\rho^2)cos2\phi$	Vertical secondary astigmatism
Z_4^4	14	4	4	$\sqrt{10}\rho^4 cos4\phi$	Vertical quadrafoil

A wavefront $W(x,y)$ can be described or rather decomposed into Zernike polynomials by

$$W(x,y) = \Sigma_{j=0}^{\infty} c_j Z_j(x,y) \tag{2.8}$$

where $Z_j(x,y)$ are the Zernike polynomials in Cartesian coordinates and c_j their respective coefficient by which they are weighted with $c_j \in \mathbb{R}$. In subsection 2.2.3 the wavefront $W(x,y)$ and how to measure it is described further.

The following table lists the first 15 Zernike polynomials by both indexing versions and shows their mathematical expression. Figure 2.3 shows how a flat-top beam's intensity changes after aberrations corresponding to the first 15 Zernike polynomials are applied and being focused by a lens. It can also be used to demonstrate how an aberrated point-spread function looks like.

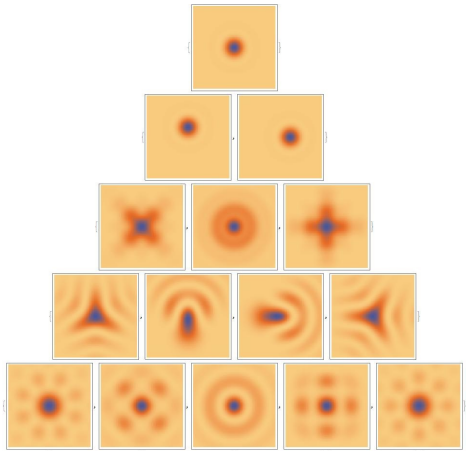

Figure 2.3: Effect of the 15 first Zernike polynomials when introduced as aberration to a flat-top beam focused by a lens. Ordered vertically by radial order n and horizontally by azimuthal degree m. Taken from [28], modified by me.

The point-spread function of a system can be used to quantify the resolution and the aberrations of an optical system. When a point source is imaged, it will, due to diffraction, not be displayed as a single point in the image plane but instead the point's intensity will spread evenly in all directions. This shape, called Airy pattern consists of a bright central region, called Airy disk, and outer rings surrounding it. For ideal optical elements, most of the intensity (about 84%) will be imaged to the Airy disk [29] and the intensity distribution looks like a 2D Gaussian. For aberrated systems, the intensity may spread more to the outer rings, thus reducing the contrast. Additionally, the PSF might spread more in one direction than the others for some aberrations, or even look cross-shaped (Astigmatism). Thus, measuring or simulating the point-spread function for specific optic elements provides insight into the quality of these elements.

2.1.3 Polarization

Polarization describes the orientation of the electric field vector $\vec{E}$ of a light wave. In homogeneous media and without being strongly focused, the field oscillates orthogonal to the propagation direction. For unpolarized light, the orientation of the field vector is random, while polarized light has a defined path. One can differentiate between linearly, circularly, and elliptically polarized light [30–32]. Before discussing specific examples of polarization states, it is essential to present the mathematical framework that describes them.

Assuming light propagating in the z-direction, and naming the other two directions H (horizontal) and V (vertical) for x and y, respectively, we can express $\vec{E}$ as:

$$\begin{aligned} E_H(z,t) &= A_H \cos(\omega t - kz + \phi_H) \\ E_V(z,t) &= A_V \cos(\omega t - kz + \phi_V) \\ \vec{E} &= \begin{pmatrix} E_H(z,t) \\ E_V(z,t) \end{pmatrix} \end{aligned} \tag{2.9}$$

where t is the time, $A_{H/V}$ and $\phi_{H/V}$ are the amplitudes and phases of the electric field for their respective directions. k and ω are the angular wavenumber and the angular frequency of the wave which describe the radians per unit distance and radians per unit time, respectively.
While k and ω are fixed, the amplitudes and the difference of the phases $\phi_V - \phi_H$ can be varied, which makes it possible for the electric field to point in different directions, thus determining the polarization. Considering time evolution of $\vec{E}$ at $z = 0$ [31]:

$$\vec{E} = \begin{pmatrix} A_H \cos(\omega t + \phi_H) \\ A_V \cos(\omega t + \phi_V) \end{pmatrix} = \Re \left\{ \begin{pmatrix} A_H \mathrm{e}^{i\phi_H} \mathrm{e}^{i\omega t} \\ A_V \mathrm{e}^{i\phi_V} \mathrm{e}^{i\omega t} \end{pmatrix} \right\} \tag{2.10}$$

where $\Re$ symbolizes the real part operation. We can define the complex amplitudes $\tilde{E_H}$ and $\tilde{E_V}$ as:

$$\begin{aligned} \tilde{E_H} &= A_H \mathrm{e}^{i\phi_H} \\ \tilde{E_V} &= A_V \mathrm{e}^{i\phi_V} \end{aligned} \tag{2.11}$$

which contain all information about the polarization state[1]. The vector $\vec{J}$ containing both complex amplitudes

$$\vec{J} = \begin{pmatrix} \tilde{E_H} \\ \tilde{E_V} \end{pmatrix} \tag{2.12}$$

is called the Jones vector [31]. It is normalized such that the intensity of the electric field I is set to 1. This is done by taking the dot product of $\vec{J}$ with its conjugate transpose $\vec{J}^\dagger$:

$$I = \vec{J}^\dagger \vec{J} = 1 \tag{2.13}$$

With a normalized Jones vector one can express polarization states in a simple manner. For horizontal polarization, where $A_V = 0$, the Jones vector has the following form:

$$|H\rangle = \vec{J_H} = \begin{pmatrix} 1 \\ 0 \end{pmatrix} \tag{2.14}$$

where $|H\rangle$ is the Bra-Ket notation of the polarization state. This means that the electric field oscillates on the horizontal axis only. Thus, for vertical polarization $|V\rangle$, $A_H = 0$:

$$|V\rangle = \vec{J_V} = \begin{pmatrix} 0 \\ 1 \end{pmatrix} \tag{2.15}$$

[1] For fully polarized light. Representation of mixed states requires the use of density matrices or Stokes vectors.

Other polarizations can then be constructed by linear combination:

$$\begin{aligned} |\Psi\rangle &= \alpha|H\rangle + \beta|V\rangle \\ |\alpha|^2 + |\beta|^2 &= 1 \end{aligned} \tag{2.16}$$

with $\alpha, \beta \in \mathbb{C}$. These factors contain the amplitude $A_{H/V}$ and phase components $\phi_{H/V}$ of the respective electric field axis. For example, if $A_H = A_V$ and $\phi_V - \phi_H = 0$ the outcome polarization has equal parts of horizontal and vertical field components and they are in phase. This polarization is called diagonal $|D\rangle$ and is polarized 45° with respect to the horizontal axis:

$$|D\rangle = \frac{1}{\sqrt{2}}(|H\rangle + |V\rangle) = \frac{1}{\sqrt{2}}\begin{pmatrix}1\\1\end{pmatrix} \tag{2.17}$$

A phase difference of π with equal amplitudes equates to anti-diagonal $|A\rangle$ polarization

$$|A\rangle = \frac{1}{\sqrt{2}}(|H\rangle - |V\rangle) = \frac{1}{\sqrt{2}}\begin{pmatrix}1\\-1\end{pmatrix} \tag{2.18}$$

All other linear polarizations are constructed by varying the amplitude difference and must have a phase difference of either 0 or π. A phase difference of $\pm\frac{\pi}{2}$ with $A_H = A_V$ is left-handed circular (+) and right-handed circular (-) polarized light. The "handedness" of these circular polarizations is a way to describe if the field vector is propagating counterclockwise (left) or clockwise (right).

$$\begin{aligned} |L\rangle &= \frac{1}{\sqrt{2}}(|H\rangle + i|V\rangle) = \frac{1}{\sqrt{2}}\begin{pmatrix}1\\i\end{pmatrix} \\ |R\rangle &= \frac{1}{\sqrt{2}}(|H\rangle - i|V\rangle) = \frac{1}{\sqrt{2}}\begin{pmatrix}1\\-i\end{pmatrix} \end{aligned} \tag{2.19}$$

Any other combination of phase and amplitudes would result in elliptically polarized light. Optical elements, which manipulate the polarization and, therefore the Jones vector, are represented by a 2x2 Jones matrix M. The general Jones matrix for a liner polarizer set at an angle θ with respect to the horizontal axis is given by:

$$M_{LP}(\theta) = \begin{pmatrix}\cos^2(2\theta) & \cos(2\theta)\sin(2\theta)\\ \cos(2\theta)\sin(2\theta) & \sin^2(2\theta)\end{pmatrix} \tag{2.20}$$

To determine the outgoing Jones vector J_o after an incoming Jones vector J_i has interacted with a Jones matrix M, one has to calculate the following:

$$J_o = MJ_i \tag{2.21}$$

Jones calculus is straightforward to use but can only describe fully polarized light. If one wants to describe partially or unpolarized light, another mathematical framework, Stokes parameters and Mueller matrices, can be used [32]. Stokes parameters only deal with the intensity of the light, meaning the phase information is lost. There are four Stokes

parameters. The first one, S_0 is the sum of intensities, while the latter three, S_1, S_2 and S_3 are the differences of intensities of orthogonal polarizations.

$$\begin{aligned} S_0 &= |A_H|^2 + |A_V|^2 = |A_D|^2 + |A_A|^2 = |A_R|^2 + |A_L|^2 = 1 \\ S_1 &= |A_H|^2 - |A_V|^2 \\ S_2 &= |A_D|^2 - |A_A|^2 \\ S_3 &= |A_R|^2 - |A_L|^2 \end{aligned} \tag{2.22}$$

where A_H and A_V are the amplitudes of the electric field like already established in 2.9. The other amplitudes are also amplitudes of the electric field but for bases with $|D\rangle$ and $|A\rangle$ (A_D and A_A) and a circular basis with $|R\rangle$ and $|L\rangle$ (A_R and A_L) as their basis vectors. S_0 is, as the sum of intensities, normalized to 1.
One can make a vector $\vec{S}$ out of the Stokes parameters called the Stokes vector.

$$\vec{S} = \begin{pmatrix} S_0 \\ S_1 \\ S_2 \\ S_3 \end{pmatrix} \tag{2.23}$$

With this vector, one can represent the polarization state of light with Stokes parameters. One can also use the parameters S_1, S_2 and S_3 to span a sphere, called Poincaré Sphere [32] seen in 2.4.

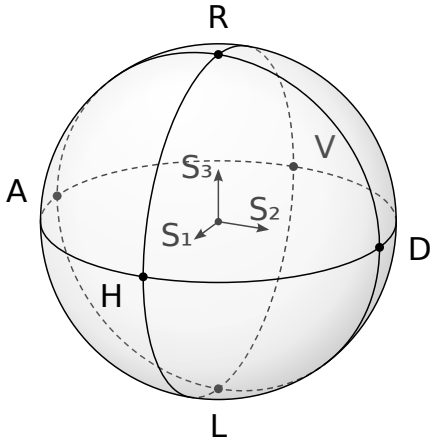

Figure 2.4: Image of the Poincaré sphere. Taken from [33].

Hereby 2ψ is the azimuthal angle on the plane spanned by S_1 and S_2 where all linear polarizations lie on. With the polar angle 2χ circular and elliptical polarizations can be reached. The third spherical coordinate, $I\rho$ is the radial distance with $0 \leq \rho \leq 1$, meaning $\rho = 0$ and $\rho = 1$ are unpolarized and fully polarized, respectively, and I the sum of intensities, usually normalized to 1. Thus, fully polarized states are mapped to a point on the sphere's surface, while partially polarized or unpolarized light would be inside the sphere. The Stokes parameters can then be expressed as:

$$\begin{aligned} S_0 &= I \\ S_1 &= I\rho\cos(2\psi)\cos(2\chi) \\ S_2 &= I\rho\sin(2\psi)\cos(2\chi) \\ S_3 &= I\rho\sin(2\chi) \end{aligned} \tag{2.24}$$

The equivalent to Jones matrices for Stokes vectors are the Mueller matrices. These are 4x4 matrices which can, analogous to 2.21 be multiplied with the Stokes vectors to calculate the effect of an optical element on a polarization state. The general Mueller Matrix for a linear polarizer set at angle θ[2] is given by:

$$M_{LP}(\theta) = \frac{1}{2}\begin{pmatrix} 1 & \cos(2\theta) & \sin(2\theta) & 0 \\ \cos(2\theta) & \cos^2(2\theta) & \cos(2\theta)\sin(2\theta) & 0 \\ \sin(2\theta) & \cos(2\theta)\sin(2\theta) & \sin^2(2\theta) & 0 \\ 0 & 0 & 0 & 0 \end{pmatrix} \tag{2.25}$$

Changing the polarization of light with optical elements like waveplates is relatively simple and polarization itself is robust when undisturbed, so it is a good way to encode information in the polarization state of photons.
For EOFLIM, the polarization of light is used to encode temporal information of the sample. In section 3.1.4 further Stokes vectors and Mueller matrices are introduced to showcase the spatial separation of the fluorescence signal in the setup.

2.1.4 Transformations

For the data analysis it is important to overlap quadrants of the EOFLIM images with each other to infer the lifetime data (further discussed in sections 3.2 and 5.1). To perform this procedure precisely, two transformations are used. Namely, Affine Transformation and Homography [34, 35]. A simple translation is not sufficient for a proper overlap of the quadrants. This might be due to the spatial separation of the light (see 3.1.4) for each quadrant, which allows the light to impinge on the camera at different angles, thus leading to variations in the projected image.
The Affine Transformation is a 2D transformation which can apply translations, shearing, scale and rotation operations to the target while keeping parallels and straight lines intact. It can be described by a 2x3 matrix M, which can be further broken down into a linear transformation (a 2x2 matrix A) followed by a vector addition (a 2x1 matrix B), i.e., a translation.
Mathematically, the Affine Transformation acts on an input vector $\vec{v_i}$ in the following way:

$$\vec{v_o} = A\vec{v_i} + B \tag{2.26}$$

[2] Again, with respect to the horizontal axis.

where $\vec{v_o}$ is the output vector[3] with

$$\begin{aligned} \vec{v_i} &= \begin{pmatrix} x \\ y \end{pmatrix} \\ A &= \begin{pmatrix} a_{11} & a_{12} \\ a_{21} & a_{22} \end{pmatrix} \\ B &= \begin{pmatrix} b_1 \\ b_2 \end{pmatrix} \\ \vec{v_o} &= \begin{pmatrix} a_{11}x + a_{12}y + b_1 \\ a_{21}x + a_{22}y + b_2 \end{pmatrix} \quad = \begin{pmatrix} x' \\ y' \end{pmatrix} \end{aligned} \tag{2.27}$$

where x' and y' are the transformed coordinates, x and y the original coordinates and $a_{ij} - b_k$ the matrix elements, each with their own effect on the vector, namely:

1. a_{11} - scaling in x-direction
2. a_{12} - shearing in x-direction
3. a_{21} - shearing in y-direction
4. a_{22} - scaling in y-direction
5. b_1 - translation in x-direction
6. b_2 - translation in y-direction

Rotations are thus applied by a combination of scaling and shearing. These six effects are also the six degrees of freedom the Affine Transformation has. To get from A and B to the 2x3 matrix M, one has to expand the vector v_i to homogeneous coordinates[4]:

$$\vec{v_i} = \begin{pmatrix} x \\ y \end{pmatrix} \rightarrow \begin{pmatrix} x \\ y \\ 1 \end{pmatrix} = \vec{v_{iH}} \tag{2.28}$$

Thus, the matrices can be combined to

$$M = \begin{pmatrix} a_{11} & a_{12} & b_1 \\ a_{21} & a_{22} & b_2 \end{pmatrix} \tag{2.29}$$

and the Affine Transformation can be written as

$$\vec{v_o} = M\vec{v_{iH}} \tag{2.30}$$

[3] Both transformations discussed in this section are implemented by an algorithm which searches for the highest correlation between the target quadrant, i.e. the input vector $\vec{v_i}$ and a template quadrant, i.e. the output vector $\vec{v_o}$, to infer the transformation matrix.

[4] Explaining homogeneous coordinates in detail would go beyond the scope of this thesis. Simply put, they are a coordinate system in projective geometry and enable the representation of Affine and other transformations as matrices by adding a non-zero scalar as third coordinate. [34]

Figure 2.5 shows an example of an Affine Transformation applied to a checkerboard. As mentioned, parallel and straight lines are kept intact, while the scale and shape of geometric objects and the angles between lines and thus orthogonality are affected. This differentiates the Affine Transformation from a pure euclidean (translation, rotation and reflection) one.

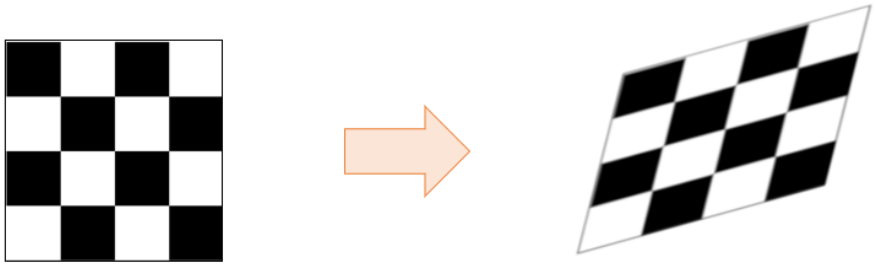

Figure 2.5: Applying an Affine Transformation to a checkerboard, rotating, shearing and scaling it. Taken from [36].

The second transformation method, Homography, is a more complicated one. It includes Affine Transformation and expands it with 2 additional degrees of freedom in the form of elation operations. These operations can be understood as coordinates being projected from one 2D plane to another one, hence Homography is also called Projective Transformation. A visual representation using a checkerboard can be seen in Figure 2.6.

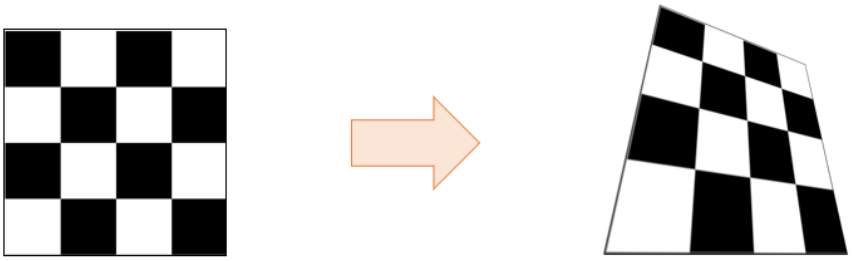

Figure 2.6: Applying a Projective Transformation to a checkerboard. Taken from [36].

Here, the checkerboard, which was on the plane of the paper before the Homography, was transformed/projected to a plane where the lower left-hand corner is going towards and the upper right-hand corner away from the reader. It is important to note that straight lines will still be straight after a Homography but parallel lines might not be parallel anymore, as is the case with this checkerboard. An everyday life example of a Homography would be the shadow cast from the wall of a building. The mathematical representation of a Homography is a 3x3 matrix. Again homogeneous coordinates have to be used:

$$H = \begin{pmatrix} a_{11} & a_{12} & b_1 \\ a_{21} & a_{22} & b_2 \\ \nu_1 & \nu_2 & 1 \end{pmatrix} \tag{2.31}$$

$$\vec{v_{oH}} = H\vec{v_{iH}}$$

where ν_1 and ν_2 are the entries affecting the elation operation[5]. Contrary to (2.30) the output vector stays in homogeneous coordinates. To convert back to Cartesian coordinates used in 2D planes, one has to divide the first two coordinates by the third. Converting (2.28) back is done by a simple division by 1. This means that the change to homogeneous coordinates in (2.28) is only done for a simpler computation and does not change the vector.
Assuming:

$$H = \begin{pmatrix} 1 & 0 & 0 \\ 0 & 1 & 0 \\ \nu_1 & \nu_2 & 1 \end{pmatrix} \tag{2.32}$$

The conversion of (2.31) would be:

$$\vec{v_{oH}} = \begin{pmatrix} x \\ y \\ \nu_1 x + \nu_2 y + 1 \end{pmatrix} \rightarrow \begin{pmatrix} \frac{x}{\nu_1 x + \nu_2 y + 1} \\ \frac{y}{\nu_1 x + \nu_2 y + 1} \end{pmatrix} = \vec{v_o} \tag{2.33}$$

This means that elation operations add these linear functions as denominators to the terms of both the x and y coordinates, thus scaling the points towards or away from the origin, just as seen in Figure 2.6 above. The simple form of (2.32) has been chosen to explicitly show the effects of the elation operation entries on an input vector. By having two additional parameters, Homography has 8 degrees of freedom, which should result in a better overlap than by using an Affine Transformation.

2.2 Optics

For this thesis, it is assumed that the reader is familiar with mirrors and lenses, which are used in everyday life and are part of introductory physics courses. In this section, less common optical elements will be introduced.

2.2.1 Beamsplitter

Beamsplitters (BS) are a crucial part of many experimental setups in optics. As their name suggests, they are used to divide a beam into two separate beams. This separation

[5]The ninth entry, 1, is insignificant, because of the arbitrary non-zero scalar mentioned in 4. The scalar can be chosen such that it cancels out this matrix element.

can be used in various fields, like interferometry, microscopy or telecommunication, where the separation - or recombination, if one reverses the pathway - is needed. In their most common form they are a cube consisting of two prisms glued together at their bases. A frequently used splitting ratio is that of a 50:50 beamsplitter, meaning that 50% of the incoming light is transmitted and 50% is reflected. Other examples for splitting ratios are 10:90 or 30:70, but any other ratio is also possible, although it might have to be custom made.
By using birefringent[6] materials [30], one can split an unpolarized beam into two linear polarizations, thus creating a polarizing beamsplitter (PBS). This means an incoming unpolarized beam is split by a PBS in such a way that the horizontal component gets transmitted, while the vertical one is reflected. By reversing the pathway, one can also recombine two beams of orthogonal polarizations.
The experiment presented in this thesis uses PBS to redirect beams of orthogonal polarizations to separate pathways, where they acquire a slight directional shift. The details will be discussed in section 3.1.4.

2.2.2 Pockels Cell

A Pockels Cell (PC) is an electro-optic component which can be used for changing the polarization of an incoming beam [37]. This is done by applying a voltage to the PC, which in turn changes the birefringence of the crystal. Birefringence is an optical property materials can have which means that the refractive index is polarization dependent. The magnitude of the difference Δn between the ordinary n_o and extraordinary n_e indices of refraction is given by

$$\Delta n = n_e - n_o \tag{2.34}$$

If Δn is positive, n_o is smaller and the direction of linearly polarized light, for which n_o is the refractive index, is the fast axis. The axis along n_e is called the slow axis. This is vice versa for a negative Δn. They are called "fast" and "slow" because a wave polarized in the fast (slow) axis direction propagates faster (slower) through the material due to the lower (higher) refractive index[7].
This difference results in an optical retardance between the horizontal and vertical electric field components of the incoming beam, which changes the polarization. The maximum optical retardance $\Delta\phi$ is achieved when the field components are aligned with the fast and slow axes and is given by the equation (2.35):

$$\Delta\phi = \frac{2\pi\ \Delta n\ L}{\lambda} \tag{2.35}$$

with L being the length of the crystal and λ the wavelength in vacuum. If the incident beam's polarization is aligned with one of the axes of the indices of refraction, the

[6] This means that the index of refraction is polarization dependent. A more detailed explanation of birefringence is given in Sec. 2.2.2.
[7] Or rather due to the lower (greater) density of the material in its path.

polarization remains unchanged.
Birefringence not only varies with direction of light polarization but also its propagation direction. The optic axis of a material describes the direction in which no birefringence is observed ($n'_e(0°) = n_o$), while maximum birefringence is present travelling perpendicular to the optic axis ($n'_e(90°) = n_e$). A material with one optic axis is called uniaxial and with two optic axes biaxial. For this thesis only uniaxial crystals are important. A beam propagating with an angle α with respect to the optic axis will be affected by an index of refraction for the extraordinary ray $n'_e(\alpha)$ as follows [38]:

$$n'_e(\alpha) = \frac{n_e\ n_o}{\sqrt{n_e^2\ \cos^2\alpha + n_o^2\ \sin^2\alpha}} \tag{2.36}$$

If the birefringence changes linearly with the applied electric field, this effect is called Pockels effect.
As mentioned above, a voltage is needed to induce the birefringence and in turn change of polarization. The voltage used to induce an optical retardance of π is called the half-wave voltage V_π. If this voltage is applied and a linearly polarized beam is incident with 45° relative to the fast and slow axes, the optical retardance will be half a wavelength and thus change the polarization to the orthogonal one, just like a half-wave plate.

The calculation of V_π is material and configuration dependent. For the Pockels Cell of the EOFLIM project, which is made out of two $LiTaO_3$ (LTA) crystals in transverse configuration, it is given by:

$$V_\pi = \frac{\lambda}{n_e^3\ r_{33} - n_o^3\ r_{13}}\ \frac{d}{2\ L} = 1306\frac{d}{L}\ V \tag{2.37}$$

where r_{ij} are material dependent electro-optic coefficients, which describe the change of the refractive indices for a specific interaction between the applied field and material [37]. For (2.37) $r_{13} = 7$ and $r_{33} = 30.3$ have been used. The indices of refraction have the values 2.179 (n_o) and 2.182 (n_e). The parameters λ, d and $2\ L$ are the wavelength in vacuum, the distance of the two electrodes and the length of the crystals, respectively. The factor 2 in front L is due to the usage of two crystals in a dual-crystal compensation scheme.
The transverse configuration and dual-crystal compensation scheme, as detailed earlier, characterize how the Pockels Cell is oriented and operated. Transverse configuration means that the electric field is applied perpendicular to the propagation direction of light. The reasoning behind using a Pockels Cell in transverse configuration are the lower capacitance and larger acceptance angles compared to longitudinal configurations [37]. Lower capacitance means shorter rise times, which is important for high frequency operations. The acceptance angle of a PC describes the angle at which incoming light is still refracted with the desired properties. As a PC is an anisotropic material, an incoming ray from outside of the acceptance angle would be affected in an undesirable way. The Bachelor's thesis of a preceding student, Nikolaos Lagos, has concluded that the angular acceptance of the PC used for EOFLIM is 67.61 mrad while the EOFLIM setup has an

aperture of 18.58 mrad. Longitudinal configurations with a higher acceptance angle are also possible but they rely on transparent electrodes, which introduce optical losses. The advantage of having two crystals with a 90° tilt between them, and therefore opposite field directions, is that it compensates for on-axis birefringence and thermal effects. LTA specifically is utilized due to its low natural birefringence[8].
The scheme of our PC can be described as follows:
Two LTA crystals of opposite orientation are placed right after each other with their long sides coated with electrodes, as seen in figure 2.7.

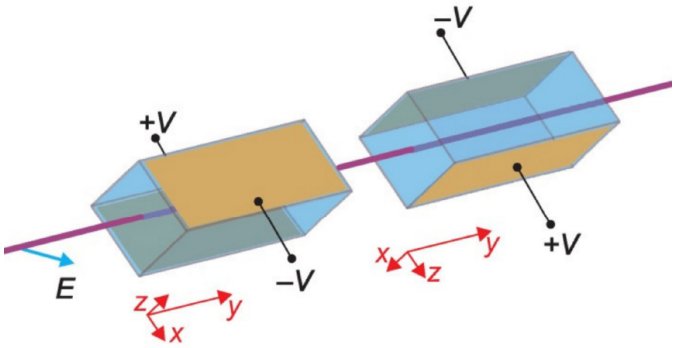

Figure 2.7: Y-cut of a double-crystal compensation scheme. Incoming light (blue) with horizontal polarization. Taken from [39].

The crystals are oriented such that incoming horizontal and vertical light are +45 and −45° relative to the z-axis, respectively. The optical axis is perpendicular to the propagation direction.
The crystals are placed on a translation stage which is used for alignment purposes and the stage itself is placed inside a casing - the Pockels Cell driver, which controls the applied voltage and repetition rate. Without any voltage applied the aforementioned crystals in opposite orientation are a zero-order waveplate and should - in theory - not affect the polarization. Inhomogeneties in the crystal might introduce errors. For a PC with applied voltage, piezoelectric ringing is another source of errors, especially for high frequencies [40].
For the EOFLIM experiments we use the PC to change one polarization to the orthogonal one. It can also be used as a fast shutter by adding a polarizer after it which would let through the incident linear polarization but completely block the orthogonal one. Generally, Pockels Cells serve both as a switchable waveplate and as signal modulators.

[8] That is the birefringence which is present without applying an electric field. It should be minimal to keep the polarization unchanged if the PC is turned off.

2.2.3 Wavefront Sensor

A wavefront sensor (WFS) consists of a microlens array and a camera, which is placed at the focal length of these microlenses. It is used to quantify aberrations in an incoming wavefront. For an ideal plane wave, each microlens would focus the light to the center of the pixels behind it (green in Fig 2.8. If the wavefront is in any way aberrated, this point will be off-center, either in x, y or both directions (red in same figure). From that, through a 2-dimensional integration process, one can infer the coefficient c_n of each Zernike polynomial, thus making a quantitative conclusion of the aberrations of the wavefront [41]. To put it in geometric terms:

$$\tan\ \alpha = \frac{\delta y}{f_{ML}} \tag{2.38}$$

with α being the incident angle on the microlens, δy the spot shift in y-direction and f_{ML} the distance between microlens and sensor, which is also the focal length of the microlens. This is likewise for δx, the spot shift in x-direction. Now, if $W(x, y)$ is the function that describes the wavefront shape, we can calculate it by integrating its partial derivatives of x and y, which are determined by δx and δy, respectively.

$$\frac{\partial}{\partial x}W(x,y) = \frac{\delta x}{f_{ML}} \quad \text{and} \quad \frac{\partial}{\partial y}W(x,y) = \frac{\delta y}{f_{ML}} \tag{2.39}$$

With the wavefront $W(x, y)$ retrieved, one can now fit it with Zernike polynomials to get the amplitude, or coefficient, c_n of each Zernike mode.

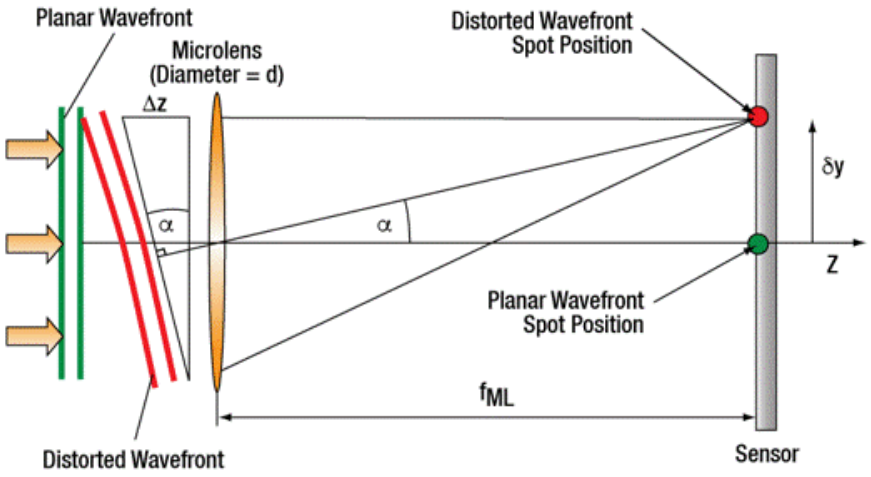

Figure 2.8: Cross section of the working principle of a wavefront sensor. Calculating the deviation of the spot to the reference spot allows one to reconstruct the wavefront. Taken from [41].

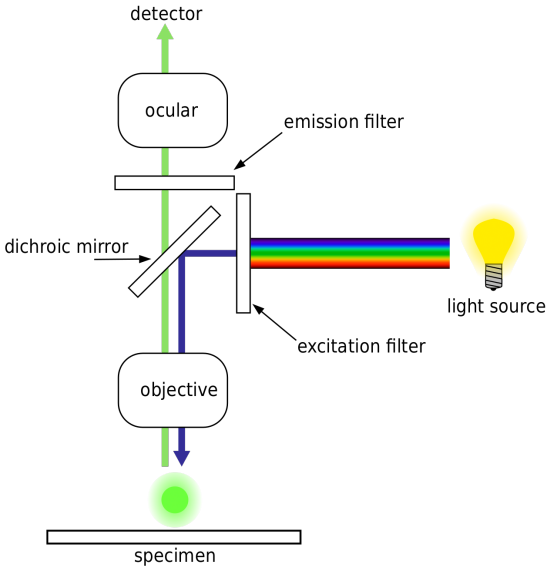

Figure 2.9: Schematic of a fluorescence microscope. Taken from [42].

2.3 Imaging

Combining physical principles and optics allows to discuss imaging methods. For this thesis, fluorescence as imaging tool is important and thus the focus of this section. Using fluorescence for microscopy can be done in different ways: For example, by measuring the intensity of the emitted photons or the lifetime of the excited state.[9] In the following, both possibilities will be explained and visualized.

2.3.1 Fluorescence Microscopy

In Figure 2.9 the schematic of a typical fluorescence microscope is displayed. Important to note are the excitation filter, which filters out the wavelengths of the white light source that are not used to excite the fluorophore, the dichroic mirror, that reflects the incoming excitation wavelength but transmits the emitted light, and the emission filter which makes sure that only the wavelengths of interest are detected [20].
The advantage of this microscopy technique is that it is versatile: Fluorophores are readily available and can be used on a wide variety of samples, making it the technique of choice for many fields like biology or medicine. Furthermore, fluorescence microscopy can be modified in ample ways, enabling more advanced techniques such as confocal microscopy, TIRF, or STED [4]. Attaching a fluorophore to a part of, e.g., a cell is called labelling. Doing that to various parts of the cell with different fluorophores (with distinct emission spectra) allows one to differentiate between them in the measurement and observe their interactions. If the different fluorophores are measured simultaneously,

[9] There is also the possibility of measuring the polarization spectrum, which will not be discussed further in this thesis.

it is called multiplexing.
This leads to the limitations of fluorescence microscopy: This technique can only be used to observe labeled or fluorescing samples. Unlabelled parts of the cell that do not experience autofluorescence or are filtered out by the emission filter are invisible with this microscope. Additionally, after a while of exposure, the ability to fluoresce weakens in fluorophores. This phenomenon is called photobleaching and results from irreversible photochemical reactions after electron excitation of the fluorophore [3, 6, 20]. These reactions alter chemical bonds in the fluorophore, resulting in, for example, a shift in the absorption spectrum or creating new, non-radiative transitions. Thus, the time to observe the sample is limited. As the number of photons is essential for this technique, it depends on fluorophore concentration, making imaging difficult where dye concentration is low.

2.3.2 Fluorescence Lifetime Imaging Microscopy

Measuring the fluorescence lifetime instead of the fluorescence intensity enables fluorescence imaging for processes that would not be visible in standard fluorescence microscopy. But before discussing these, the measurement of lifetime should be explained.

Time and Frequency Domain Lifetime measurements are done in one of two domains: Time or frequency domain [3, 7, 8, 20, 43]. In these domains, there are again different ways of measuring, but the principle is the same. In the time domain, one can use TCSPC, where the photon's arrival time is checked against the laser pulse to infer the delay between excitation and emission. A pulsed laser, or rather illumination, is necessary for time domain lifetime determination. Important to note is that the emission signal is a convolution between the excited state decay and the excitation pulse. Thus, as seen in Figure 2.10, short pulses are necessary.
Another way to measure in the time domain is by taking two snapshots of the same fluorophore with a known time difference (time-gating). From there, one can extrapolate the exponential decay of the excitation and thus determine the lifetime.
On the other hand, in frequency domain, a continuous wave (CW) laser is used to illuminate the samples. Determining lifetime in this domain is done by modulating the source's intensity and measuring the emitted waveform's corresponding phase shift. To clarify: Exciting an atom with a theoretical lifetime of $\tau = 0$, the emission would be instantly visible after excitation - with the same frequency and an indistinguishable waveform to the source. The fluorescence lifetime retards the emission, thus, causing a phase shift. The longer the lifetime, the bigger the phase shift. Additionally, the lifetime causes signal demodulation, which also increases with the lifetime. Therefore, in frequency domain FLIM, one can define two lifetimes, which are equal to each other for single exponential processes, namely the phase lifetime and modulation lifetime. Keeping in mind Eq. (2.1), one can express the phase lifetime by:

$$\phi = \arctan(\omega\tau) \tag{2.40}$$

and the modulation lifetime by,

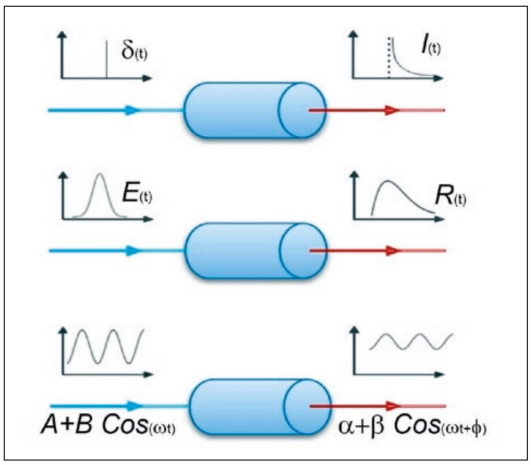

Figure 2.10: Exciting a fluorescent sample (cylinder) with different excitation pulses (blue) results in different emissions (red). A delta excitation (top) gives an emission with exponential time decay, while a broad excitation (middle) results in a broadened emission. The response to a sinusoidal-modulated excitation (bottom) is a sinusoidal emission with a phase shift and different modulation in amplitude and average signal. Taken from [7].

$$M^2 = 1/(1 + (\omega\tau)^2) \tag{2.41}$$

where ϕ is the phase, M the modulation and ω the angular frequency. Phase, as well as modulation lifetime, can be seen at the bottom of Figure 2.10.

Confocal laser scanning vs. Wide-field microscopy Two main acquisition methods are utilized to determine the lifetime. The most common commercial FLIM systems acquire images by scanning the whole field of view (FOV) pixel-by-pixel with a focused excitation beam. The detection of photons and thus the retrieval of lifetime information is done by the aforementioned TCSPC. Scanning FLIM produces high-resolution images with a very good signal-to-noise ratio (SNR) but is limited by acquisition speed and cost. For a sample of 128x128 pixels, only 6 frames per second can be achieved by one of the fastest commercially available scanning FLIM setups [9].
Wide-field microscopy, in contrast, is usually cheaper and achieves faster acquisition rates by illuminating the whole FOV simultaneously. The fastest commercial systems can take 20 frames per second for an image of 1008x1008 pixels [10]. However, the cameras used for wide-field FLIM suffer from drawbacks like photon losses when the detector is inactive, as it is the case for gating the signal with the camera, high read noise or low quanutm efficiency (39% for [10]). Both time and frequency domain FLIM are utilized with wide-field microscopy.
Advantages and Disadvantages The advantages and limitations of FLIM in comparison

to fluorescence microscopy should now be discussed: Contrary to fluorescence intensity, the fluorescence lifetime of a fluorophore is insensitive to concentration, thus enabling measurements in environments where concentration is unequal. Additionally, since lifetime depends on physicochemical and biochemical parameters like pH, temperature, oxygen, or calcium concentration, it provides more information about biomolecular interactions and intracellular processes [3, 20]. For example, one can - in real time - monitor the change in lifetime within a cell depending on a chosen parameter by calibrating it with a curve (lifetime against chosen parameter). With Fluorescence Microscopy similar characterizations can be made but due to the dependence on fluorophore concentration the results are more difficult to interpret. Furthermore, the molecular environment can be inspected more clearly with FLIM as it can differentiate between fluorophores, which emit at the same wavelength but have different lifetimes due to the parameters mentioned above. Moreover, photobleaching affects the measured intensities directly while the lifetime is only indirectly affected through noise.
The significant drawback of FLIM compared to fluorescence microscopy is the complex and more specialized equipment and data analysis. Instead of a straightforward measurement of the fluorescence intensity with photomultiplier tubes or avalanche photodiodes and thus acquiring the needed information, one has to use single-photon detectors for the TCSPC technique as mentioned above, somehow gate the incoming signal extracting the lifetime through specialized software or perform hetero-/homodyne detections of the frequency domain FLIM signal. This also leads to a more time-consuming data analysis. Another limitation is the reduced spatial resolution compared to other microscopy techniques specializing in super-resolution.

2.4 Collaborations

Although the following two subsections also fit under section 2.3, they are separated because these are the imaging techniques and the goals of our collaborators for which the EOFLIM project is optimized.

2.4.1 5-ALA guided brain surgery

Brain tumors, malignant or benign, need to be surgically removed to ensure the well-being of the patient. This is done by a neurosurgeon resecting the tumor. In doing so, it is important that neither too little nor too much is removed, as the tumor may grow back or the patient may suffer from permanent brain damage. Thus, to differentiate between healthy tissue and the brain tumor, real time-microscopy is needed to guide the neurosurgeon.
Consequently, a technological challenge arises: A technique is needed which is fast, can objectively quantify tissue and can effectively work with a small range of angles, high background light and a long working distance [13]. For that, they chose FLIM as their microscopy technique due to the limitations other techniques have.
For example, while Raman spectroscopy [44] has a high molecular sensitivity, it suffers

from a low photon yield, and ambient light in the operating room would disturb the measurements. Additionally, as real-time imaging is crucial for guidance in the operating room, the long acquisition times of 10 minutes [45] render this technique completely ineffective.
Another imaging approach which does not suffer from these technical limitations is narrow band imaging [46], which has been used to guide biopsies of brain tumors by detecting the increased neovascularization of the tumor. However, the diffuse tumor borders do not exhibit this kind of neovascularization [47], making this technique unattractive for our collaborators.
Lastly, fluorescence microscopy could be considered. It is already used in the area of brain surgery. What it does lack, is the specificity, i.e. objective quantification, between healthy tissue and the brain turmor. Due to autofluorescence, i.e. naturally occurring fluorescence in healthy brain tissue, the neurosurgeon might mistake it for the tumor. This can be overcome by using FLIM instead, as the lifetime between them differs. Advantages of FLIM over fluorescence microscopy have been discussed in a previous section 2.3.2. For the specific case of brain surgery, they also include the following:
As the brain is a thick sample, the tissue can absorb or scatter a lot of the excitation as well as the emitted light, therefore decreasing the detected intensity and obscuring the tumor. Through the lifetime measurement, one can still see the whole area of glioma tissue. Furthermore, there is a type of tumor called low-grade gliomas (LGG), which naturally fluoresce weaker than high-grade gliomas (HGG) and are therefore harder to resect during fluorescence microscopy. Additionally, ambient light in the operating room is eliminated as only parts of the signal with the same frequency as their reference signal get amplified for frequency-domain FLIM. For time-domain FLIM, the short duration of the measurement makes it inconsequential. The difference between fluorescence microscopy and FLIM for brain surgery is shown in Figure 2.11.

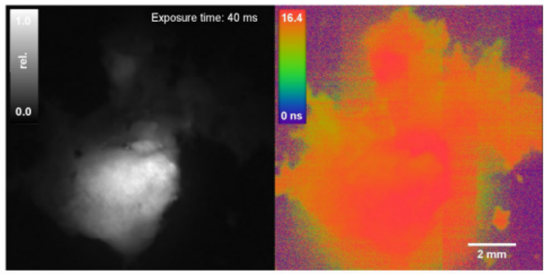

Figure 2.11: Left: A greyscale fluorescence microscopy image. The fluorescing part is a tumor. Right: The same FOV but now a FLIM image. The tumor (red) is more visible by lifetime detection. Taken from [14].

The collaborators of the AKH, led by Dr. Unterhuber in Vienna, use frequency domain FLIM for their measurements [13–17]. To make the tumor visible, they use 5-ALA guided surgery:
For this method, the patient is orally administered 5-ALA, which is converted to Proto-

porphyrin IX (PPIX) and consequently to Heme. While PPIX is a fluorophore, Heme is not fluorescent as it includes a ferrous iron complex, which quenches the fluorescence. It is believed that the conversion from PPIX to Heme cannot take place in gliomas due to the missing enzyme ferrochelatase, which leads to a high concentration of fluorescent PPIX molecules in the brain tumor, thus making it visible for FLIM imaging during brain surgery.
During the collaboration, the EOFLIM setup will be compared to the FLIM systems of the AKH.

2.4.2 SR-SIM

SR-SIM is the abbreviation for super-resolution structured illumination microscopy. Super-resolution means that the resolution of the microscope is increased beyond Abbe's diffraction limit. This limit describes the minimum distance d between two resolvable points. For a microscope with a wavelength λ propagating through a medium with index of refraction n and half-angle θ, d is given as:

$$d = \frac{\lambda}{2n\ \sin\theta} = \frac{\lambda}{2\ NA} \tag{2.42}$$

where NA is the numerical aperture of a system, which describes the range of angles for which a system accepts or emits light. For modern microscopes, NA can increase to 1.4 by immersing the objective in oil with a high refractive index (1.52). Using green light with $\lambda = 500\ nm$ and $NA = 1$ thus results in a minimum distance between two resolved points of $d = 250\ nm$. SR-SIM utilized a technique which decreases d beyond the diffraction limit:
It operates by illuminating the (fluorescing) sample with a known interference pattern, thus convolving the unknown sample pattern with the aforementioned interference fringes [48, 49]. This leads to a raw image with a so-called Moiré pattern. This pattern consists of two different patterns, where one of them has a lower periodicity than the sample and illumination patterns and its associated frequency can be resolved with ease, while the other one has a higher periodicity and its associated frequency is most likely not resolvable by the detector. But, by knowing the frequency associated with the illumination pattern and the frequency associated with the lower periodicity of the Moiré pattern, one can reconstruct the sample pattern, getting a resolution increase of factor 2 [48–50] compared to the frequency associated with the illumination pattern[10]. By setting this frequency to the diffraction limit, one can achieve super-resolution images.
Of course, this reconstruction is not done by a single image but rather by moving the illumination pattern around (translation and rotation) and taking several images. For a 2D-SIM reconstruction, 9 images are needed - 3 translations, each with 3 rotations. For 3D images, one needs 5 translations, thus bringing the count to 15 images [48–50].

Figure 2.12 shows the schematic of an SR-SIM microscope and some pattern examples. To create the illumination pattern, a movable diffraction grating is inserted in the excitation

[10] For a detailed explanation as to why linear SIM can only increase resolution by a factor 2, see [50].

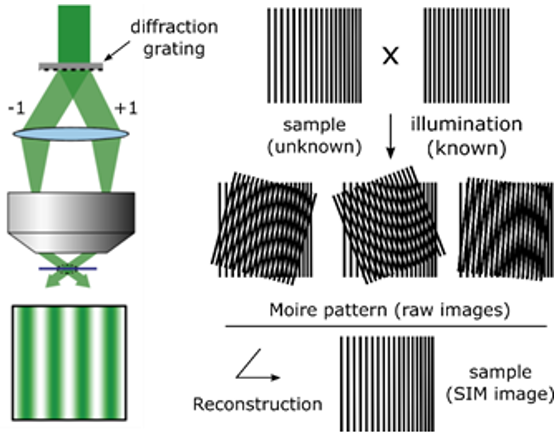

Figure 2.12: Schematic of a structured illumination microscope. Taken from [48].

path. By allowing zeroth and/or first-order beams to pass further through the optics, they interfere at the focal point, thus forming the wanted pattern. The Moiré pattern can be expressed mathematically in the following way:
Assuming $\cos(k_1 x)$ describes the sample pattern with frequency k_1, and $\cos(k_2 x)$ likewise for the illumination pattern, their addition is the Moiré pattern given in eq. (2.43)

$$\cos(k_1 x) + \cos(k_2 x) = 2\cos(\frac{k_1 x + k_2 x}{2})\cos(\frac{k_1 x - k_2 x}{2}) \tag{2.43}$$

where $\cos(\frac{k_1 x - k_2 x}{2})$ is the pattern with the lower frequency used for the reconstruction.
An advantage of SR-SIM is that it increases resolution in x,y and z-directions simultaneously, not to mention the speed of this technique compared to other super-resolution techniques, which arises from only needing 9 (15) images for 2D (3D) images, which is a substantial amount fewer than other techniques (e.g. STORM needs thousands of frames [51]). Additionally, conventional and readily available fluorophores can be used. Drawbacks of SR-SIM are that its increase in resolution is not as good as other techniques ($\sim$ 100 nm for SR-SIM vs. $\sim$ 20 nm for STORM) and that the reconstruction can introduce artifacts to the image. To conclude, the advantages of SIM make it ideal for live-cell imaging and, as a wide-field microscope, a good method to pair with EOFLIM.

3 Setup

After establishing the means to talk about FLIM microscopes, now the method used in this thesis, namely the electro-optic FLIM (EOFLIM) setup, is discussed.

3.1 Working principle

From section 2.4 about the collaborations it is clear that EOFLIM needs to be fast to capture footage in real time for brain tumor surgery but it also must be sensitive enough to acquire super-resolution data of molecules. Speed and sensitivity are the advantages of wide-field FLIM and scanning FLIM, respectively. Thus, EOFLIM has to combine them to be suitable for the collaborations.

To maintain the needed speed, EOFLIM must acquire data from the whole FOV simultaneously. But using wide-field FLIM cameras comes with aforementioned drawbacks regarding noise and quantum efficiency. Thus, an idea would be to replace this camera with a conventional scientific camera. Consequently, the lifetime data has to be inferred differently but it would mean an increase in sensitivity and quantum efficiency.
EOFLIM does exactly this by gating the signal that reaches the camera, in front of the camera and imaging the un/gated signals to different parts of the sensor. Therefore, the specifications of the chosen camera are the limitations of this technique, making it more sensitive than wide-field FLIM and faster than scanning FLIM. The camera used as of writing this thesis is the Prime BSI from Teledyne Photometrics which allows EOFLIM to take 1024x1024 pixels images with 63 frames per second and a quantum efficiency of 92% at 575 nm. This is compared to the wide-field FLIM mentioned in 2.3.2, three times faster with more than double the quantum efficiency.

The following subsections will explain in detail how the EOFLIM system works, each focusing on a different aspect of the whole setup.

3.1.1 Illumination

The sample is fixed on a coverlip in the standard wide-field microscope. The laser is directed through an objective to the sample. The resulting fluorescence light is then collected by the same objective, transmitted through the dichroic, and imaged to a plane conjugate to the sample plane (CSP). From there it gets collimated through an achromats and then enters the first polarization splitting system. The path from here on is shown in Figure 3.1 and described in the following subsection 3.1.4.

The wide-field microscope described in this subsection, also displayed in the aforementioned figure, is interchangeable with any wide-field microscope as the EOFLIM setup is a box that can be attached to various wide-field microscopes as a module. As long as the image produced by the predecessor wide-field microscope is focused on the CSP[1], the EOFLIM box can use this image as a sample. Attaching the EOFLIM box to the SR-SIM of our collaborators is also how SR-EOFLIM is achieved.

3.1.2 Synchronisation

To synchronize the laser pulses with the Pockels Cell, a small fraction of the illumination beam is outcoupled by a half-silvered mirror to a photodiode, which sends a pulse to a delay generator. This delay generator sends a pulse to the Pockels Cell electronics to apply the voltage to the PC at the right time. This means the PC is triggered by a laser pulse that has already passed through. This is inconsequential because the laser pulses arrive in a specific time interval, thus enabling a precise alignment of the PC trigger to the next pulse.

3.1.3 Gating

Using the fact that a Pockels Cell can change the polarization of light from horizontal to vertical and vice versa, one can split these polarizations spatially, thus gating the beam in unchanged polarization (ungated) and changed polarization (gated) light. Through the spatial separation, they arrive at different parts of the camera.

3.1.4 Spatial separation of polarizations

To separate polarizations, one can use polarizing beam splitters and mirrors. The EOFLIM setup, displayed in Figure 3.1, utilizes two so-called "polarization splitting systems" - from now on called PSS. The unpolarized emission from the sample (grey) arrives at the first PSS, where it gets split into horizontal (red) and vertical (blue) polarization. Then, both beams hit a mirror, respectively. These mirrors redirect the beams to another PBS, however, at small opposite angles with respect to the optical axis. After the PBS, further propagation will lead to spatially separated images in the Pockels cell with the horizontal beam being on top of the vertical one. Now, following the horizontal beam and assuming a Pockels Cell without applied voltage, the beam gets focused through a tube lens on the Pockels Cell plane inside the PC. A cross section of the PC plane is visible in Figure 3.1b. As no voltage is applied, the beam continues unchanged. The propagation of the beam continues; the beam gets collimated through a second tube lens and arrives at the second PSS. The unchanged horizontal beam is transmitted by the first PBS and hits another mirror, which shifts the beam slightly to the left. From there, it is transmitted by the second PBS of the second system, is focused by a second achromat, and hits the camera in the upper (shift from the first system) left-hand (shift from the second system) quadrant. On the other hand, the vertical beam is reflected by

[1] Which has an angular spread of less than 18.58 mrad

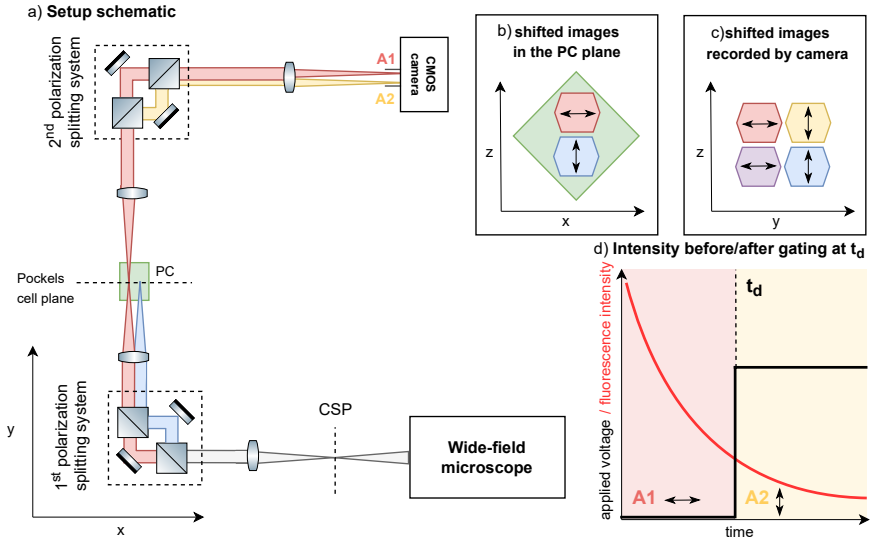

Figure 3.1: a) Schematic of the EOFLIM setup. For clarity, after the Pockels Cell only the path of the initially horizontal beam is shown. The schematic does not feature the excitation path to the wide-field microscope. b) Cross section of the PC plane featuring the horizontal and vertical components (beams) of the emission beam. c) Cross section of the camera plane featuring two ungated (red, blue) and two gated (yellow, violet) quadrants. d) Intensity for the top channel before and after gating at t_d. Taken from Nele Jarnots Bachelor Thesis, modified by me.

both PBS of the second system and acquires a shift slightly to the right. Thus, it hits the camera in the lower (shift from the first system) right-hand (shift from the second system) quadrant. By applying the correct voltage to the PC, one can change the polarization of the incoming beams, thus changing the shifts they get from the second system. So, the initial horizontal beam turns vertical (yellow) and acquires the shift to the right from the second PSS, therefore hitting the camera at the upper right-hand quadrant. The opposite happens for the initial vertical turned horizontal beam (violet in c)), and it arrives in the lower left-hand quadrant. As both quadrants in the upper half of the image stem from the same, initially horizontal beam, they are called the top channel, while the lower quadrants are the bottom channel. Data analysis is done separately for each channel. Figure 3.1c also displays a cross section of the camera plane. Using Stokes Vectors and Mueller matrices, the path from unpolarized beam to the individual quadrants can be described. First, the needed vectors and matrices shall be explained:

Stokes vectors The needed Stokes vectors are $\vec{S_0}$, $\vec{S_H}$ and $\vec{S_V}$, which are unpolarized, horizontally and vertically polarized light, respectively.

$$\vec{S_0} = \begin{pmatrix} 1 \\ 0 \\ 0 \\ 0 \end{pmatrix}; \vec{S_H} = \begin{pmatrix} 1 \\ 1 \\ 0 \\ 0 \end{pmatrix}; \vec{S_V} = \begin{pmatrix} 1 \\ -1 \\ 0 \\ 0 \end{pmatrix} \tag{3.1}$$

Polarizing Beamsplitters Polarizing Beamsplitters have two matrices. One for transmission BS_T and one for reflection BS_R. As a Polarizing Beamsplitter wants to transmit only horizontally polarized light and reflect vertically polarized light, one can describe these two matrices with the ones of the respective linear polarizers:

$$BS_T = \frac{1}{2}\begin{pmatrix} 1 & 1 & 0 & 0 \\ 1 & 1 & 0 & 0 \\ 0 & 0 & 0 & 0 \\ 0 & 0 & 0 & 0 \end{pmatrix}; BS_R = \frac{1}{2}\begin{pmatrix} 1 & -1 & 0 & 0 \\ -1 & 1 & 0 & 0 \\ 0 & 0 & 0 & 0 \\ 0 & 0 & 0 & 0 \end{pmatrix} \tag{3.2}$$

Mirrors Mirrors with ideal reflectivity for all polarizations are assumed. To include the end positions on the camera plane, which does not change the polarization, in the calculation, an index *up*, *low*, $left$ or *right* is included for each mirror. The Mueller matrix for a mirror is:

$$M_x = \begin{pmatrix} 1 & 0 & 0 & 0 \\ 0 & 1 & 0 & 0 \\ 0 & 0 & -1 & 0 \\ 0 & 0 & 0 & -1 \end{pmatrix} \tag{3.3}$$

Where x is one of the four indices. The last two entries on the diagonal of the mirror matrix are -1, because mirrors do change the handedness of polarized light.

Pockels Cell The matrix of a PC is that of a general linear retarder M_{GLR}:

$$M_{GLR} = \begin{pmatrix} 1 & 0 & 0 & 0 \\ 0 & \cos^2(2\theta) + \sin^2(2\theta)\cos(\delta) & \cos(2\theta)\sin(2\theta)(1-\cos(\delta)) & \sin(2\theta)\sin(\delta) \\ 0 & \cos(2\theta)\sin(2\theta)(1-\cos(\delta)) & \cos^2(2\theta)\cos(\delta) + \sin^2(2\theta) & -\cos(2\theta)\sin(\delta) \\ 0 & -\sin(2\theta)\sin(\delta) & \cos(2\theta)\sin(\delta) & \cos(\delta) \end{pmatrix} \tag{3.4}$$

here, θ is the angle of the beam to the fast axis and δ the retardance between fast and slow axis, as can be calculated with (2.35). Without voltage, and thus no retardance ($\delta = 0$) and an angle of $\theta = 45°$, one would get the 4x4 identity matrix $I_4 = PC_{Off}$. Applying the correct voltage changes the retardance to $\delta = \pi$. So the matrix for the ideal case with $\theta = 45°$ and $\delta = \pi$ is:

$$PC_{On} = \begin{pmatrix} 1 & 0 & 0 & 0 \\ 0 & -1 & 0 & 0 \\ 0 & 0 & 1 & 0 \\ 0 & 0 & 0 & -1 \end{pmatrix} \tag{3.5}$$

The mathematical description for the unchanged horizontal part of the beam, which ends up in the upper left-hand quadrant is:

$$\vec{S_{up,left}} = BS_T\ M_{left}\ BS_T\ PC_{Off}\ BS_T\ M_{up}\ BS_T\ \vec{S_0} \tag{3.6}$$

To calculate it step-by-step:
First, the unpolarized beam hits the first PBS of the first PSS, where the beam is split in two.

$$\begin{aligned} BS_T\ \vec{S_0} &= \frac{1}{2}\begin{pmatrix} 1 & 1 & 0 & 0 \\ 1 & 1 & 0 & 0 \\ 0 & 0 & 0 & 0 \\ 0 & 0 & 0 & 0 \end{pmatrix}\begin{pmatrix} 1 \\ 0 \\ 0 \\ 0 \end{pmatrix} = \frac{1}{2}\begin{pmatrix} 1 \\ 1 \\ 0 \\ 0 \end{pmatrix} &= \frac{1}{2}\ \vec{S_H} \\ BS_R\ \vec{S_0} &= \frac{1}{2}\begin{pmatrix} 1 & -1 & 0 & 0 \\ -1 & 1 & 0 & 0 \\ 0 & 0 & 0 & 0 \\ 0 & 0 & 0 & 0 \end{pmatrix}\begin{pmatrix} 1 \\ 0 \\ 0 \\ 0 \end{pmatrix} = \frac{1}{2}\begin{pmatrix} 1 \\ -1 \\ 0 \\ 0 \end{pmatrix} &= \frac{1}{2}\ \vec{S_V} \end{aligned} \tag{3.7}$$

It is important to note that the intensity is split in two in this step, which is symbolised by the fraction $\frac{1}{2}$ in front of the two resulting vectors $\vec{S_H}$ and $\vec{S_V}$. To focus on one path, $\vec{S_V}$ is disregarded now.
Following the horizontal path, the next optical element encountered is a mirror, which reflects the beam without changing the polarization but shifting the beam slightly up:

$$M_{up}\ \frac{1}{2}\vec{S_H} = \begin{pmatrix} 1 & 0 & 0 & 0 \\ 0 & 1 & 0 & 0 \\ 0 & 0 & -1 & 0 \\ 0 & 0 & 0 & -1 \end{pmatrix}\ \frac{1}{2}\ \begin{pmatrix} 1 \\ 1 \\ 0 \\ 0 \end{pmatrix} = \frac{1}{2}\ \vec{S_{up}} \tag{3.8}$$

The next element is a PBS, again. As the PBS transmits 100% of the incoming horizontal polarization, the vector is unchanged. This holds true for all other elements following the path. Through a second mirror in the path, another shift ($left$) is applied. Thus, the final vector from Eq. (3.6) is:

$$\vec{S_{up,left}} = \frac{1}{2}\begin{pmatrix} 1 \\ 1 \\ 0 \\ 0 \end{pmatrix} \tag{3.9}$$

The paths of the other three quadrants are:

$$\begin{aligned} \vec{S_{up,right}} &= BS_R\ M_{right}\ BS_R\ PC_{On}\ BS_T\ M_{up}\ BS_T\ \vec{S_0} \\ \vec{S_{low,right}} &= BS_R\ M_{right}\ BS_R\ PC_{Off}\ BS_R\ M_{low}\ BS_R\ \vec{S_0} \\ \vec{S_{low,left}} &= BS_T\ M_{left}\ BS_T\ PC_{On}\ BS_R\ M_{low}\ BS_R\ \vec{S_0} \end{aligned} \tag{3.10}$$

3.1.5 Acquisition modes

Data acquisition happens in two modes. Fast FLIM and FLIM Sweep.
The main difference between the two modes is the quantity of snapshots in time taken during acquisition. For Fast FLIM, only one image is taken[2]. For bi-exponential lifetimes, more timestamps of the decay are needed, which is exactly what our second acquisition mode, FLIM Sweep, does. Additionally, Fast FLIM images are taken for a specified time delay t_d between triggering pulse and gating of the PC (visible in Figure 3.1d), while for FLIM Sweep t_d is changed (swept) in a range of 120ns[3], thus making it possible to see a change in intensity ratio (see Eq.(3.12) below) in time. This is corresponding to Eq. (2.1), and allows, through fitting, to infer the lifetime τ. For FLIM Sweep the Pockels Cell is turned on each frame for a finite gating time t_g[4]. Figure 3.2 shows the sweeping of t_d in 4 phases.

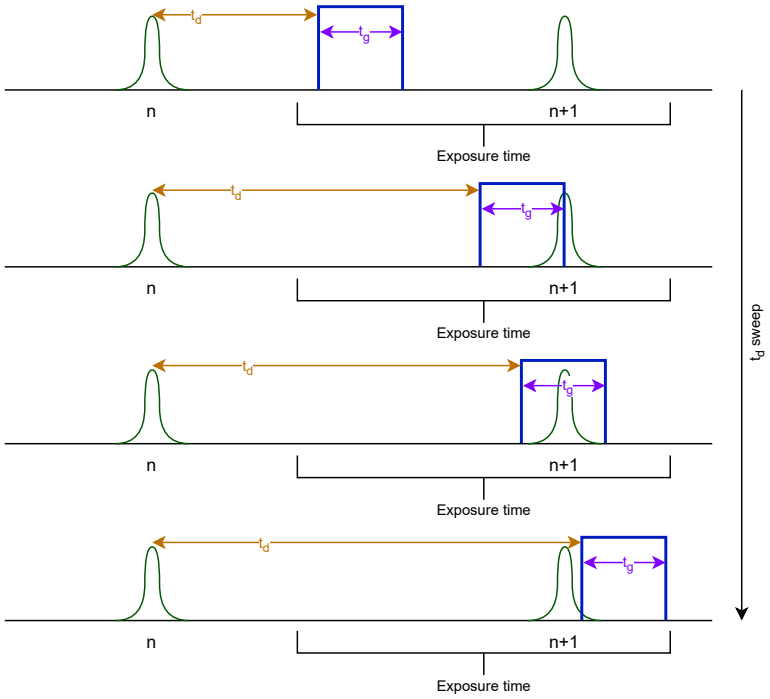

Figure 3.2: Sketch of the FLIM Sweep sweeping of t_d. Green: Laser pulses; Blue: Gating window; Violet: Gating time t_g; Orange: Time delay t_d. Not drawn to scale.

1. Phase 1: The Pockels Cell is triggered shortly after the triggering pulse n. All photons of pulse n+1 arrive at the ungated quadrants, the intensity ratio $R_I \approx 0$.

[2] Of course, if a video shall be recorded with the EOFLIM setup, multiple Fast FLIM images are taken in quick succession.
[3] For 300 frames with a delay of 0.4ns for each frame.
[4] Usually 60 ns.

2. Phase 2: The PC is triggered shortly before pulse n+1, but the gating time t_g is long enough to gate the first half of incoming photons. $R_I \approx 0.5$.

3. Phase 3: t_d and pulse n+1 are in sync. All photons arrive at the gated quadrants. $R_I \approx 1$.

4. Phase 4: The PC is triggered after almost the whole n+1 pulse already passed the PC. $R_I \approx 0.1$.

Of course these 4 phases are only an overview of all possible pulses and t_d intervals.

To summarize: Fast FLIM takes a single frame of the exponential decay, thus can only yield accurate results for mono-exponential lifetimes. It can be used to generate videos. FLIM Sweep on the other hand acquires multiple frames, allowing it to additionally be used for bi-exponential decays. For a noisy image with mono-exponential decay it is thus better to use FLIM Sweep to acquire more data.
Both modes share the acquisition of the IRF, the Instrument Response Function, which, as the name suggests, describes the response of the instruments, meaning detector, optics and electronics, to the laser with no sample present. In other words, it serves as a calibration tool as it corresponds to the reaction of a fluorophore with an infinitesimal lifetime. The number of acquired IRF frames, n, equals the number of FLIM Sweep frames.

3.2 Workflow & Data analysis

Figure 3.4, displays a workflow flowchart for both acquisition modes and their respective post-processing. The subsections 3.2.2 and 3.2.3 shall explain the flowchart step by step. But before that, the principle and creation of the Lookup Table (LUT) shall be explained for clarity.

3.2.1 Lookup Table

The LUT is a tool used to infer the lifetime information of images acquired with Fast FLIM. It is a list of pre-calculated intensity ratios for various lifetimes τ. After acquiring the singular Fast FLIM image, its ratio R_i for each channel i is calculated and then compared pixel-by-pixel to the LUT. The lifetime of the most similar ratio of the LUT is then assigned as the lifetime for the sample pixel. The creation of the LUT can be described as follows:
First, the IRF of the system is acquired for the same time delay t_d as the corresponding sample. To get the maximum ratio variation, t_d should be chosen such that the fluorescent signal is partially gated. Thus, photons impinge on both quadrants on the camera, making it possible to calculate the total T_i and ratio R_i of intensities of both quadrants:

$$\begin{aligned} T_i &= U_i + G_i \\ i &= top, bottom \end{aligned} \tag{3.11}$$

where U_i and G_i are the ungated and gated quadrants of the respective channel i. Subsequently, the ratio images R_i are calculated:

$$\begin{aligned} R_i &= \frac{G_i}{T_i} \\ i &= top, bottom \end{aligned} \tag{3.12}$$

which normalizes the intensities and also removes any disturbances by photobleaching or laser power fluctuations.
Calculating the IRF ratio pixel-by-pixel[5] gives the starting point for the ratio calculations of the LUT as the IRF is equivalent to the response of a fluorophore with infinitesimally short lifetime ϵ. The theory of the ratio calculation of the LUT is the following: We assume an ideal step-function, which is 0 before t_d and 1 from t_d to infinity as the gating of the PC. The incoming horizontal fluorescence signal, given by equation (2.1) is then split into two intensities. The first one, I_{HH}, is for the ungated quadrant where the PC is turned off and goes from 0 to t_d:

$$I_{HH} = \int_0^{t_d} I_0 \exp^{-\frac{t}{\tau}}\, dt = -\frac{I_0}{\tau} \exp^{-\frac{t}{\tau}} \Big|_0^{t_d} = -\frac{I_0}{\tau}(\exp^{-\frac{t_d}{\tau}} - 1) \tag{3.13}$$

The second one, I_{HV}, are the photons arriving in the gated quadrant, now vertically polarized as the PC turned on at t_d until infinity:

$$I_{HV} = \int_{t_d}^{\infty} I_0 \exp^{-\frac{t}{\tau}}\, dt = -\frac{I_0}{\tau} \exp^{-\frac{t}{\tau}} \Big|_{t_d}^{\infty} = \frac{I_0}{\tau} \exp^{-\frac{t_d}{\tau}} \tag{3.14}$$

Using the results of (3.13) and (3.14) for (3.12) gives:

$$R = \frac{\exp^{-\frac{t_d}{\tau}}}{\exp^{-\frac{t_d}{\tau}} - \exp^{-\frac{t_d}{\tau}} + 1} = \exp^{-\frac{t_d}{\tau}} \tag{3.15}$$

which is the theoretical model for the ratio calculation where τ is usually varied 1000 times in increments of 0.01 ns to infer 1000 different ratios, which are saved in the LUT. The actual calculation has to consider the convolution of the ideal decay with the experimental IRF.
Now the LUT can be used to compare it to the ratio of the sample data, which is calculated as seen in (3.12). Figure 3.3 shows the IRF and a couple of calculated ratios. In the appendix 7.10 an example lookup table[6] can be found.

[5] Due to Pockels Cell inhomogeneities, the values might differ for each pixel. By doing pixelwise calculations, the LUT can more precisely match the sample ratios.
[6] For this example lookup table the ratio has been varied from 0 to 1, instead of the lifetime.

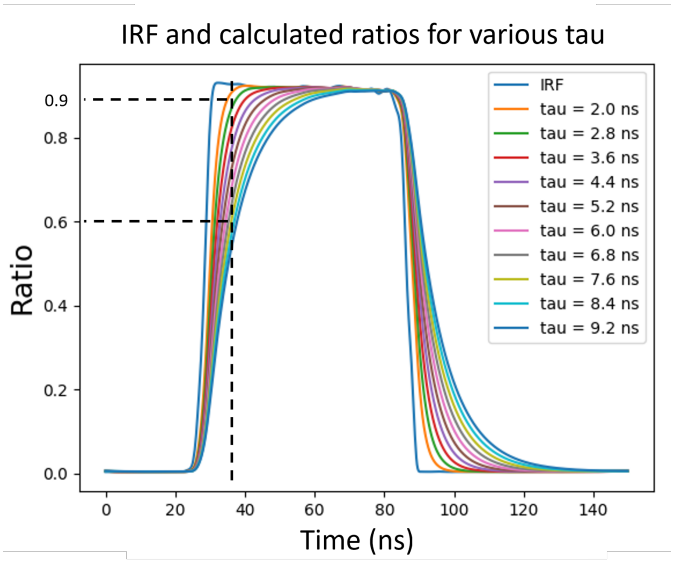

Figure 3.3: The ratio as a function of time for the IRF and various lifetimes τ. Two lifetimes, $\tau = 2.0$ ns and $\tau = 7.6$ ns are highlighted with their respective ratios $R = 0.9$ and $R = 0.6$. Taken from the presentation of [52].

3.2.2 Fast FLIM

Beginning with Fast FLIM, as stated in the previous subsection 3.1.5, a singular image of the sample is taken at a specified t_d from which the lifetimes will be calculated. But before that, a sweep of n IRF frames is taken. The double-sided arrow between both acquisition methods at the IRF box symbolizes that this step is identical for both modes. These two steps form the acquisition part of the Fast FLIM mode.
The data analysis then starts by overlapping the sample image channel-wise, i.e., both upper quadrants (top channel) and both lower quadrants (bottom channel) are overlapped and analyzed separately. The used transformation matrix is saved for usage in the next step[7]. After overlapping, the same script then calculates the total T_i ((3.11)) and ratio R_i ((3.12)) images. Both of these images are then used in a later step.
As both channels go through the same post-processing, the distinction between them is omitted from now on.
Afterwards, the IRF is also overlapped, using the same transformation matrix. The resulting IRF ratio image, also calculated with Eq. (3.12), is immediately used for the next step: Creating a LUT. Then, using the ratio image from the sample and checking it against the LUT gives the corresponding lifetime for each pixel, which is saved as a lifetime image. Combining the lifetime image with the total image of the sample - the inner workings of this script as well as the overlapping scripts are further described in

[7]Either by saving it as a .npy file or by including the sample image in the next step to infer the same matrix again

chapter 5 - yields the final lifetime-intensity image.

3.2.3 FLIM Sweep

The acquisition of the FLIM Sweep mode starts identical to Fast FLIM by taking an IRF stack of n frames. Following, a sample is placed in the wide-field microscope and n frames with increasing t_d are acquired as a sample stack file. This concludes the acquisition part of FLIM Sweep.
The first data analysis step looks very similar to the one from Fast FLIM, but the main difference is that the overlapping script needs a frame of the sample stack with almost equal intensity distribution in each quadrant as a template for inferring the most accurate transformation matrix (template frame). As in Fast FLIM, the transformation matrix is saved for the IRF Overlap and Total as well as Ratio images are calculated by using Eq. (3.11) and (3.12), respectively. As the double-sided arrow for the next step symbolizes, it is identical to the one from Fast FLIM. The next step infers the lifetime values of each pixel for each frame by using a reconvolution fitting method [19]. Meaning that the IRF is convolved with a mono- or bi-exponential function of the form

$$f(x) = A \exp^{-\frac{t}{\tau}} + B \tag{3.16}$$

or

$$f(x) = A \exp^{-\frac{t}{\tau_1}} + B \exp^{-\frac{t}{\tau_2}} + C \tag{3.17}$$

respectively, and then this convolved decay is varied in its parameters until it fits optimally to the ratio data of the sample. The resulting lifetime is saved as a lifetime image, which is, as in Fast FLIM, then combined with the total image of the sample to yield the final image.

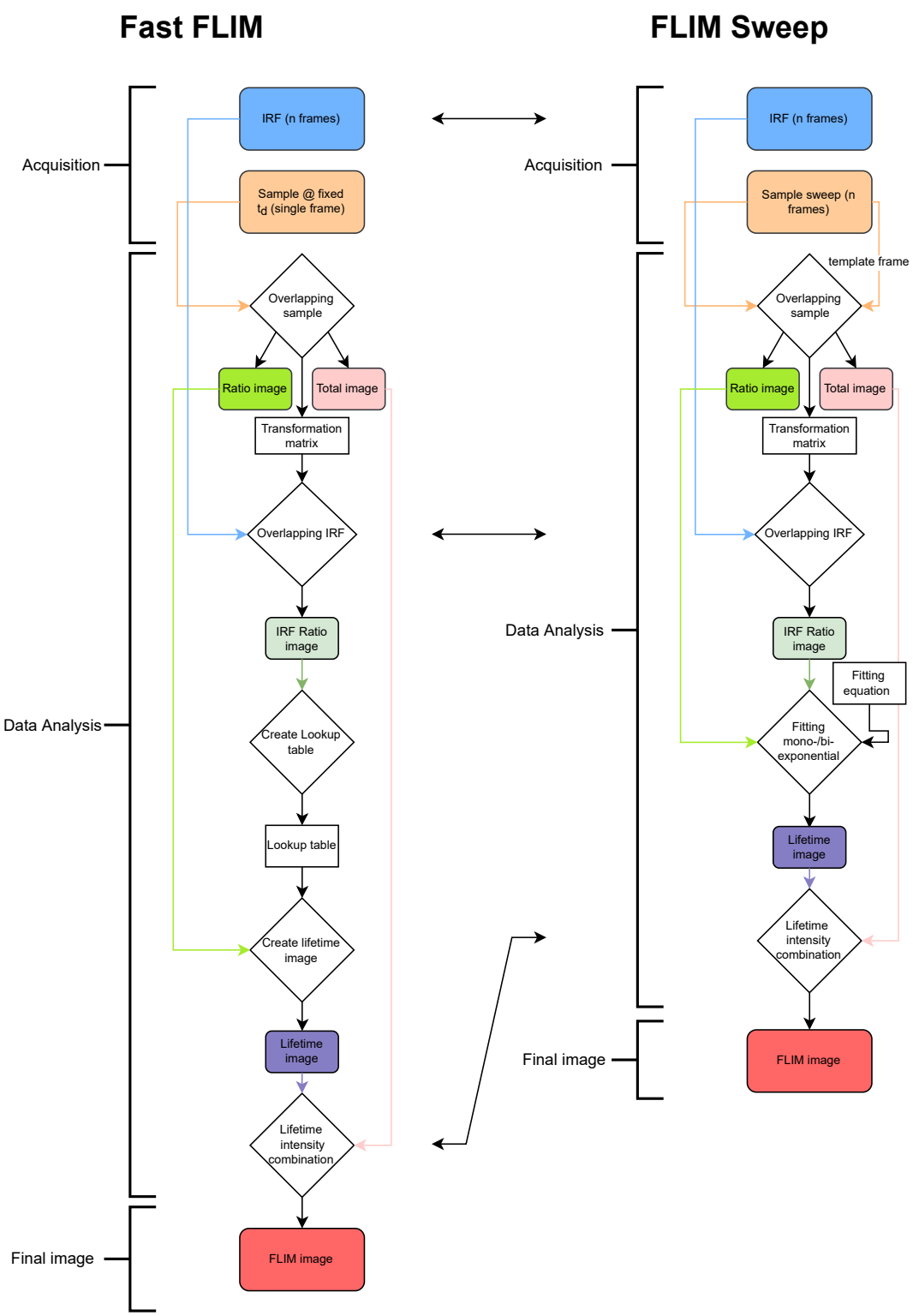

Figure 3.4: Flowchart of the Workflow of both acquisition modes. Squares with round edges: Images; Squares: Matrices; Diamonds: Scripts; Double-sided arrows: Identical step for both modes

4 Setup Optimization

As it is crucial for super-resolution imaging to have an aberration-free optical system, the EOFLIM setup had to be optimized to prepare it for the collaboration with the Huser Group in Bielefeld. In total, three groups of optical elements had to be inspected. The PBS, the lenses near the sample and image plane, and the achromats in front and behind the PC. A different procedure has been chosen for each of them, as they were more suitable for that element or easier to implement. The lenses at the sample and image plane have been discussed in Nele Jarnot's Bachelor thesis, while the other groups form the focus of this chapter.

4.1 Wavefront sensing

The wavefront sensor was chosen to inspect the aberrations created by the PBS as it has been identified that the aberrations were worse in the quadrants where the beams have been reflected by them compared to the one where it has been transmitted all the time. The difference was also visible between the beams that were reflected and transmitted compared to the initial vertically polarized beam that stayed vertically and therefore got reflected 4 times.
With the wavefront sensor, it was expected to see higher Zernike coefficients and thus aberrations in the reflected path.

4.1.1 Small FOV Experiment

The experimental setup is shown in Figure 4.1. The simple setup consists of a laser, Thorlabs KLS635, a mount for the PBS and two translation stages. Only one stage is necessary but for a faster experimental process two were used. On top of the stage the wavefront sensor WFS20-5C by Thorlabs has been mounted together with an ND filter to protect the sensitive sensor.
While measuring the transmitted path, a cap is screwed on the reflection path of the PBS for laser safety and the wavefront sensor is placed on the translation stage in the transmitted path, vice versa for measurements of the reflected path. As the wavefront sensor is very sensitive to misalignment, the translation stage has to be used to align it and thus greatly reduce the Zernike coefficients c_2 and c_1 for the aberrations X/Y-Tilt, respectively. An average over 10 measurements was acquired and taken as result. This has been repeated for both transmitted paths (PBS used as labelled on top of the cube and PBS upside down, using the other side of the reflective coating) of all 4 PBS, then the wavefront sensor got placed on the second translation stage and all reflected paths of the 4 PBS got measured.

Albeit the results, discussed in a later section 4.3, did show a difference between transmitted and reflected paths, the beam only illuminated a small part of the PBS, thus a qualitative conclusion for the whole cubes was not possible through this experiment.

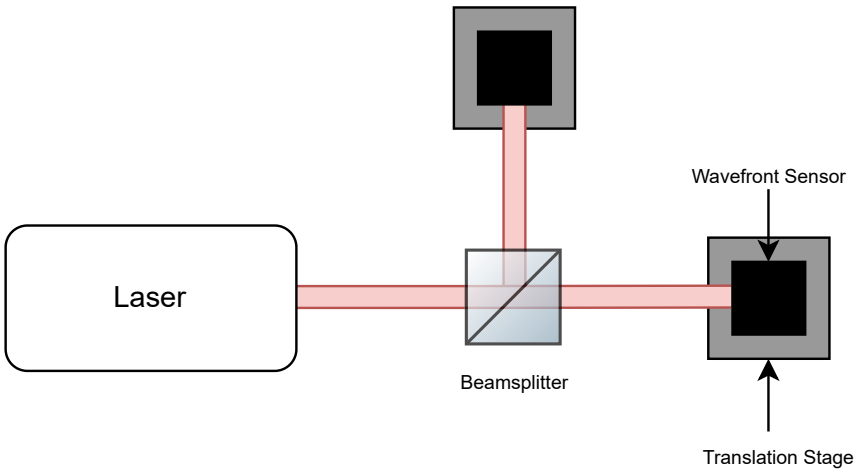

Figure 4.1: Schematic of the first wavefront sensor experiment.

4.1.2 Full PBS FOV

To measure the entire field of view of the PBS, the setup was changed such that two telescopes were included:
One was after the laser to expand the beam to the desired size, and one was in front of the wavefront sensor, as the sensor was smaller than the PBS, so the beam had to be demagnified. The schematic for this experiment can be seen in Figure 4.2. The problem with this setup is that four extra optical elements had to be included for the two telescopes compared to the other setup. This introduced aberrations, which had to be negligible compared to the ones introduced by the PBS. Calibrating the sensor to the beam without a PBS in the path was tricky, as it had to be aligned very precisely, and even touching anything in the setup introduced X/Y-Tilt aberrations again, ruining the calibration. Using the translation stage to reduce X/Y-Tilt again would also not recover the calibration as the alignment had to be too precise. Additionally, creating a new wavefront reference for the reflected path was impossible without using one of the PBS or substituting it with a mirror, which would, again, introduce unwanted aberrations.
Thus, after measuring some of the transmitted and reflected paths, it has been discussed and decided to stop this experiment due to time constraints and experimental difficulties.

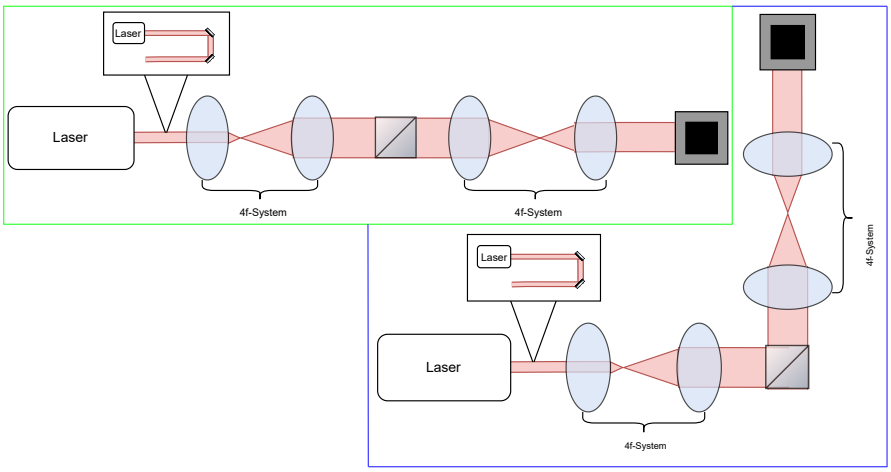

Figure 4.2: Schematic of the full PBS FOV wavefront sensor experiment. Green box: Transmitted path; blue box: Reflected path. Small boxes symbolize that the laser had to be redirected as obstacles were on the optical table.

4.2 Zemax Simulations

Zemax Simulations were done as Thorlabs made the black box files[1] of their tube lenses available. The files for the achromats used at that time were also at hand such that a qualitative comparison could be made. Simulations were done for two settings: First, for a path without an objective, just with a point source, and secondly with an objective at the beginning to simulate our system more precisely. In Figure 4.3, the version with the objective can be seen. The setup is as follows: After the objective, the sample (here, a point) gets focused such that a lens placed at a focal length distance can collimate the sample. From there the beam hits a mirror which changes the direction of propagation by 90° to the black box or achromats. Afterwards, the beam gets focused to what would be the PC plane and as it expands again, interacts with the second black box or achromat. The setup ends with another mirror and lens to focus the beam at the "detector". To simulate the EOFLIM system even better, the mirrors were given a slight tilt, thus imitating the spatial separation. The simulation would yield the point-spread function for these parameters, which have been compared.

The results of these measurements will be discussed at a later point. What is important to mention is that there have been several more simulations with tube lens files from other companies like Olympus, Nikon, or Zeiss, but these are unofficial files found on the internet. Since the companies do not grant access to the actual files, the unofficial files were excluded for the final decision of replacing the achromats.

[1] These are files where the user cannot see what is happening but the simulation can correctly calculate results with them.

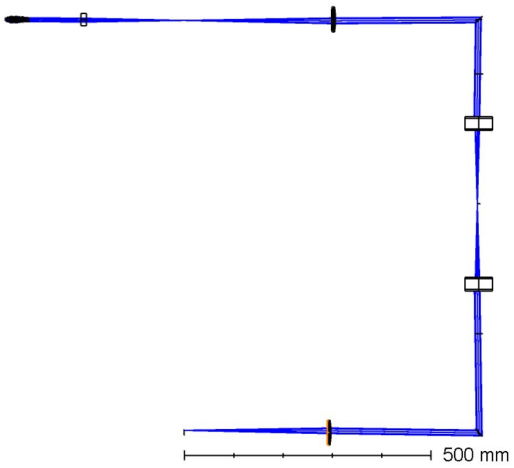

Figure 4.3: 2D view of the optical path of the simulation, starting with an objective in the upper left-hand corner.

4.3 Results

In this section, the results of the setup optimization experiments and simulations are shown and discussed.

4.3.1 Wavefront sensor

For most aberrations, the Zernike coefficients were 0 for the transmitted and reflected paths. But as expected, two aberrations, namely oblique and vertical astigmatism, c_3 and c_5, respectively, were higher for the reflected paths. Figure 4.4 displays bar graphs for both aberrations. What is important to note is the fact that the PBS labeled as BS2 exhibits higher aberrations not only in the reflected but also the transmitted paths, therefore reducing the overall quality of the final image. It is also important to reiterate that these results are only true for a small fraction of the PBS aperture.

4.3.2 Zemax simulations

The resulting PSFs, displayed in Figure 4.5, show that the Thorlabs tube lenses (right) are better than the achromats (left) used before, as the Strehl ratio is 0,980 compared to 0,927. This means more of the collected light is correctly focused on the Airy disk instead of spreading to the outer rings. A Strehl ratio of 1 is the theoretical limit and means that all the light is correctly focused. Through the slight mirror shift introduced in the simulation, the PSFs are elongated at an angle.

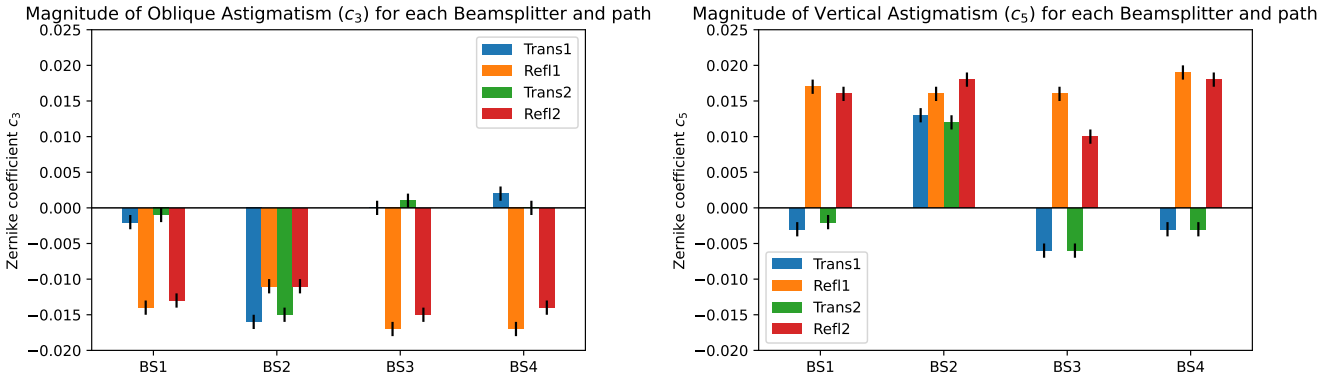

(a) Values of Zernike coefficient c_3

(b) Values of Zernike coefficient c_5

Figure 4.4: Results of the Zemax simulations, with an objective and introduced mirror tilts.

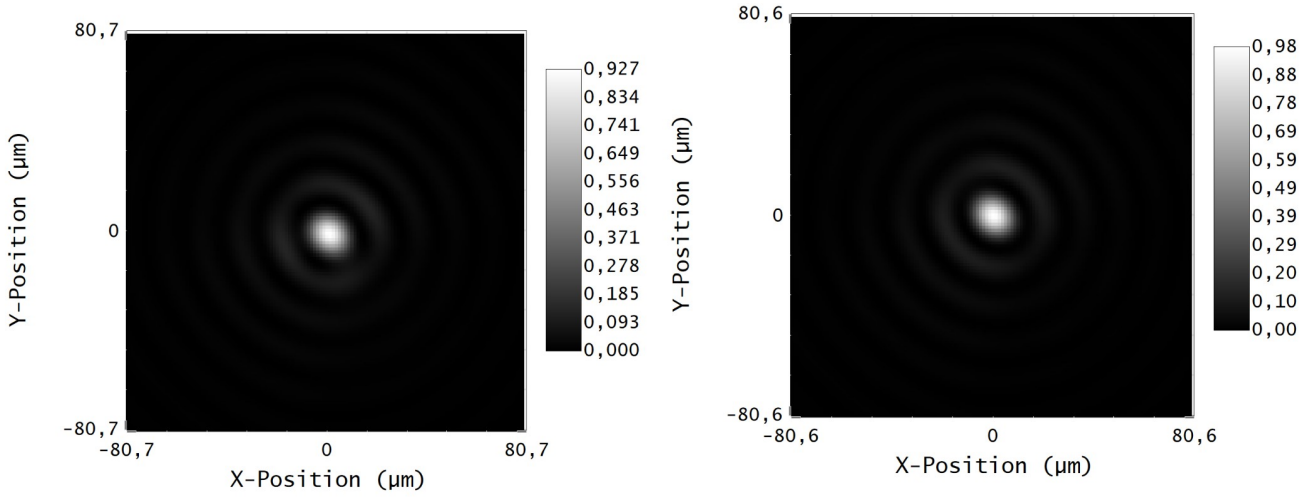

(a) Simulated PSF of the achromats.

(b) Simulated PSF of the Thorlabs tube lenses.

Figure 4.5: Zemax Simulations comparing the achromats (left) to the Thorlabs tube lenses (right). The elongation of the point-spread function is due to an applied shift through mirrors used in the simulation to approximate the experiment.

4.3.3 Conclusion

After the wavefront experiments and the Zemax simulations have been conducted, new beamsplitters as well as the Thorlabs tube lenses have been bought. This, combined with the replacement of 1-inch achromats for 2-inch achromats, resulted in less aberrated particles in all 4 quadrants.
Figure 4.6 shows a before (left) and after (right) picture. Important to note is that the

particles in the after picture are slightly elongated in one direction depending on their polarization. This can be countered by positioning a quarter waveplate before the first achromat.

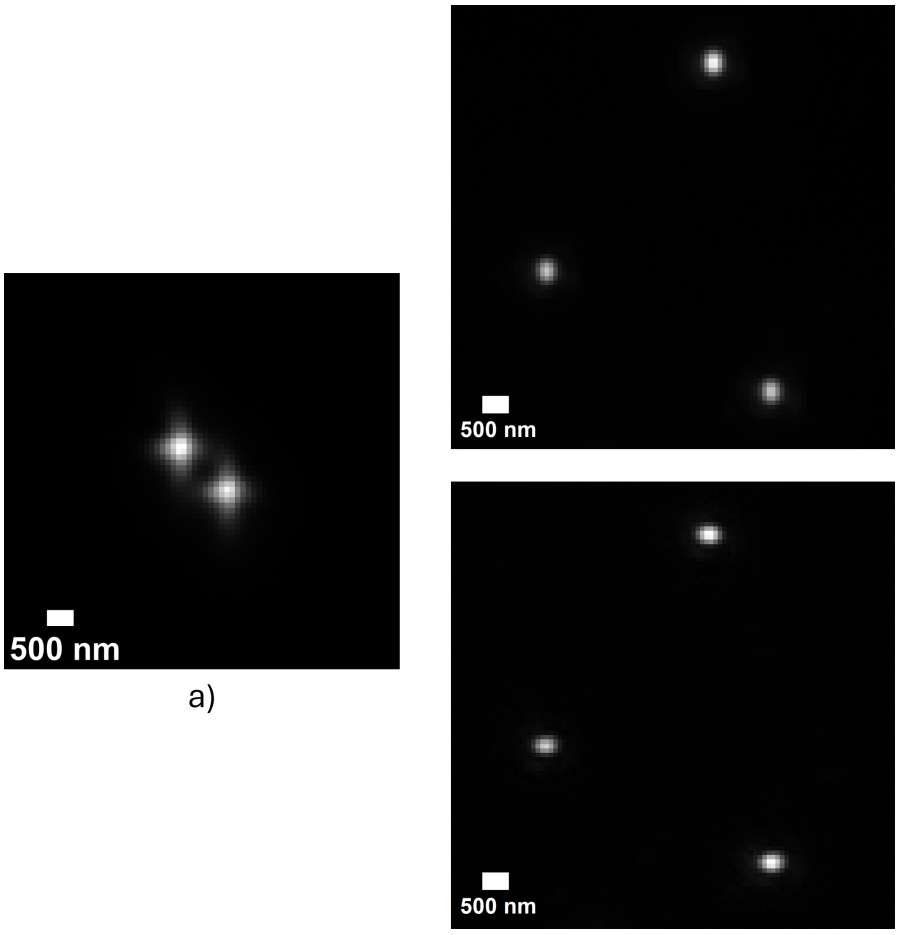

Figure 4.6: Before (left, pixel size 103.2 nm, 63x magnification) and after (right, pixel size 77.4 nm, 84x magnification) changing the optics, thus reducing the aberrations. The imaged beads are FluoSpheres™ Carboxylate-Modified Microspheres, 0.17 µm, orange fluorescent (540/560), 2% solids.

5 Data analysis improvement

Just like setup optimization, data analysis is a vital part in getting good and meaningful results from an experiment. In this chapter, the improvement of the data analysis and how it evolved is discussed.
The most refinements have been done to increase the accuracy of the analysis, but an increase in speed and convenience for the experimenters is also mentioned.

5.1 Overlapping Script

The first part of the data analysis is to overlap the quadrants of each channel. Thus, an error or imprecise result in this part of the analysis will propagate and yield inaccurate lifetime estimations. Hence, it is of utmost importance to get an accurate overlap of sub-pixel precision. Even more, considering that this microscope shall be used for a super-resolution imaging collaboration.
Before describing the algorithm in detail, one question shall be answered.
Why not just overlay both quadrants without running a correlation algorithm?
Because humans cannot perfectly align mirror tilts and a camera with a sample, especially for super-resolution experiments. And even if that were possible, shifts of the optical elements mentioned above happen over time due to many factors like temperature, pressure on the optical table, etc. For such sensitive work, a correlation and overlapping script saves a lot of time, which would be used for re-alignment instead.

5.1.1 Working principle of the Script

The framework of the script is the following: The input image gets split such that each quadrant is now a separate image of equal size. From there, the transformation matrix is inferred by a correlation algorithm - or in older versions, by providing the script with 3 points per quadrant, which shall be overlapped to a template image. This transformation matrix - one for each quadrant - is saved in a variable and applied in a transformation function together with the target quadrant for each frame. Again, for each frame, the ratios as well as totals are calculated (see Eq. (3.12) and Eq. (3.11)) and stacks (putting quadrants of the same frame after each other in a .tif-file) are created. In the last step, each output image is saved to a separate file in the same folder. As the script has undergone ample changes since its beginnings, the specifics of each step changed over the script's lifetime. Still, the framework of splitting the input image, inferring a transformation matrix, applying the matrix, calculating and saving the results is version unspecific.

5.1.2 Evolution of the script

Affine Transformation The basic functions were already present when improving this script became a task. Namely, reading and saving the images, as well as the first form of an overlapping transformation, the Affine Transformation by OpenCV. As this transformation has six parameters, one has to provide 3 points of each image to calculate the matrix and thus transform the images. In the first implementation, this was done by clicking on 3 different spots on a template image and each quadrant, such that every quadrant could be aligned with the template (which is one of the quadrants) and therefore, with each other. Figure 5.1 shows the procedure for one quadrant and the template.

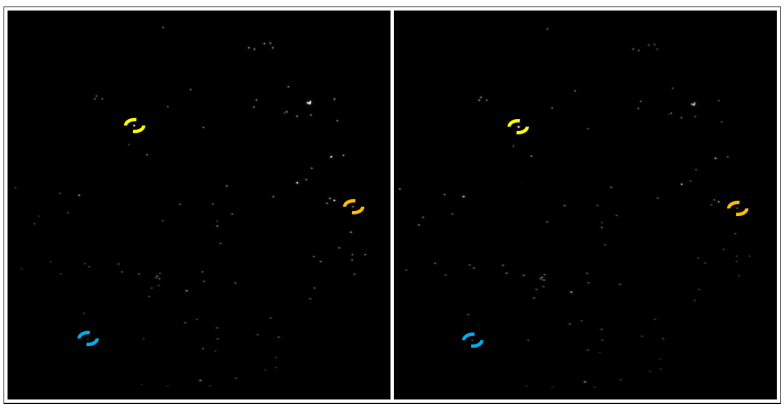

Figure 5.1: Showcasing the old overlapping technique by clicking on specific points on a quadrant (left) and then on the same points on the template (right) to align them. The colored circles indicate the chosen particles for the transformation.

This script was updated with a Gaussian fit for particles and was eventually split up into two scripts to save the resulting transformation matrix to a file and reuse it for different samples. Although the performance and speed of this procedure improved as a result of the changes, a systematic error in the code persisted, which limited the precision. With the super-resolution collaboration the need for a more precise and faster version arose.

Using a Correlation Algorithm To achieve that, the idea was to eliminate the transformation matrix by clicking altogether and substituting it with a correlation algorithm. The chosen algorithm was the ECC algorithm by OpenCV.

1. Enhanced Correlation Coefficient Algorithm The Enhanced Correlation Coefficient Algorithm by OpenCV was first proposed in the 2008 paper "Parametric Image Alignment Using Enhanced Correlation Coefficient Maximization" [53] by Georgios D. Evangelidis and Emmanouli Z. Psarakis from the University of Patras. In the paper, they explain what the ECC exactly is: It is a variation of a correlation coefficient enhanced by the fact that it is invariant to photometric distortions like contrast and brightness changes.

This enhancement is done by using the zero-mean vectors of the intensity profiles and dividing (nomralizing) them by their euclidian norm, making them invariant to bias and gain and thus photometric distortions [53]:
Assuming $I_t(x)$ and $I_w(y)$ are the intensity profiles of the template and warped images, respectively and $x = [x_1, x_2]^t$ and $y = [y_1, y_2]^t$ their coordinates. Then a set of coordinates $T = \{x_k, k = 1, ..., K\}$ in the template frame exists which, through the ECC, shall be mapped to corresponding coordinates in the warped image. This mapping can be described by $y = \phi(x : p)$ with $p = [p_1, ..., p_N]^t$ being a vector of unknown parameters which shall be estimated. Now, we can define the intensity vectors i_t $i_w(p)$ as:

$$\begin{aligned} i_t &= [I_t(x_1), I_t(x_2), ..., I_t(x_k)]^t \\ i_w(p) &= [I_w(y_1(p)), I_w(y_2(p)), ..., I_w(y_k(p))]^t \end{aligned} \tag{5.1}$$

Subtracting both vectors with their respective arithmetic mean results in the zero-mean vectors $\bar{i_t}$ and $\bar{i_w}(p)$, which is invariant to bias. The performance of the transformation is examined with the objective function $E_{ECC}(p)$:

$$E_{ECC}(p) = \left\| \frac{\bar{i_t}}{\|\bar{i_t}\|} - \frac{\bar{i_w}(p)}{\|\bar{i_w}(p)\|} \right\|^2 \tag{5.2}$$

Minimizing (5.2) is equal to maximize the enhanced correlation coefficient $\rho(p)$:

$$\rho(p) = \frac{\bar{i_t}^t \bar{i_w}(p)}{\|\bar{i_t}\| \|\bar{i_w}(p)\|} = \hat{i_t}^t \frac{\bar{i_w}(p)}{\|\bar{i_w}(p)\|} \tag{5.3}$$

where $\hat{i_t}^t = \frac{\bar{i_t}^t}{\|\bar{i_t}\|}$ is a constant.
The algorithm tries to maximize the ECC by breaking the alignment problem down, approximating to secondary optimizations, and iterating over them [53].

This algorithm improved the results in precision and speed. Namely, instead of creating a transformation matrix and then using it, which would take about 5 minutes, one can use the raw image as input, wait approximately 02:30 minutes, and have an output with sub-pixel accuracy. Additionally, this algorithm can be used to do Homography, as well as Affine Transformation.
Although better and faster than before, another promising algorithm, TurboReg, was considered and tested. This algorithm began as an ImageJ plugin, a program used by many scientists in the field of biomedical imaging, and later on, it was released as its own package for Python called pystackreg.

2. TurboReg Algorithm The algorithm used for the TurboReg functions is based on the Marquardt-Levenberg algorithm for nonlinear least-square optimization [54] and was first introduced by the paper "A Pyramid Approach to Subpixel Registration Based on Intensity" [55] from the year 1998 by Thévenaz et al. It uses a coarse-to-fine iterative

strategy, meaning that it first roughly aligns a low-resolution version of the images, which is gradually refined until it reaches the desired resolution. Alignment itself happens with the aforementioned strategy of minimizing the least square intensity difference between these two images, or rather their spline representation [55].

TurboReg was slightly more precise than ECC for specific samples. It was observed that TurboReg performed better if the template quadrant (in this case always the ungated one) was brighter than the other one, so a statement got added to the script that checks the sum of intensities of both quadrants first and assigns the brighter one as template. The actual application of TurboReg's transformation was slower and sometimes the output data got corrupted while saving, so it was decided to take the Homography matrix the TurboReg algorithm inferred and use the transformation function of the ECC algorithm to apply the matrix. This proved to be faster and bug-free.

Creating different versions From this point on, the two versions, ECC and TurboReg+ECC, split into many different scripts, all with the same structure and framework but different inputs for the scientists' convenience. Additionally, as both versions proved to be more precise for images where beads or multiple smaller signal sources are present, there is a script version for both algorithms where the transformation matrix is calculated by taking a single frame of such an image and is then applied to a full stack of an image with, for example, cells on it.

Multiprocessing vs. Multithreading The latest improvement was the addition of multiprocessing to the scripts. This did not work well; most operations in these overlapping scrips are Input/Output operations with minimal CPU load. Multiprocessing should be used for more CPU-heavy tasks while threading can manage these I/O tasks faster. Comparing the same script for the same data for a multiprocessing, a threading and the standard[1] version, reveals that the threading version, where all tasks are done through threading, is, with an average time of 210.12 s, the fastest version, followed by the standard version with 214.8 s and the multiprocessing version with 225.162 s on average. The complete data can be found in table 7.3 in the appendix.
The newest versions of each script can be found on the GitHub of the Juffmann Group[2].

5.2 Combination script

After using the overlapping script, which outputs the ratio and total images of each channel, and calculating the lifetime image through the LUT or the reconvolution fit, one can combine the lifetime image with the total image to get a lifetime-intensity image:
First, the total image is normalized from 0 to 1 and then used to create a transparency mask, meaning that depending on the pixel intensity, the mask is, in certain places, completely opaque (intensity = 0), completely transparent (intensity = 1), or between

[1] There have been single tasks that have not been done through threading or multiprocessing before.
[2] For access, please contact Thomas Juffmann under Thomas.juffmann@univie.ac.at.

these two maxima, gradually increasing with intensity values. Applying this mask to the displayed lifetime image is crucial as the low-intensity background areas of the captured image appear very noisy in the lifetime image, due to shot noise. This noise is suppressed as the mask is almost completely opaque in those areas, thus making it barely visible. After application of the mask, one has to create two colormaps, in RGB and greyscale, respectively. The RGB map is applied to the lifetime image, while the greyscale one is used for the intensity, i.e., the transparency mask. For a specified lifetime range, the values are mapped equidistantly to the colors going from blue over green to red. In terms of the HSV color model[3], lifetime is represented by the "hue" of the color, while intensity is corresponding to the "value", which can also be called brightness.

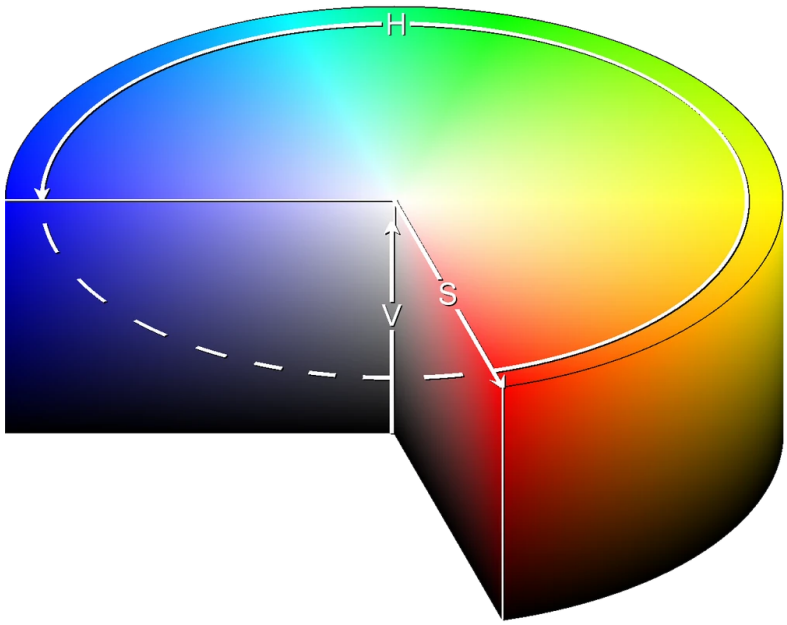

Figure 5.2: A representation of the HSV color model cylinder. H = Hue, S = Saturation, V = Value. The missing 120° are exactly the colors we do not use for mapping. Important to note is that the arrow of H is inverted for our purpose, meaning that we use blue for the lowest and red for the highest lifetimes. Taken from [56]

Figure 5.2 shows a visual representation of the HSV color model. As seen, hue is the angle of the cylinder, while value is the height. The third parameter, saturation, is the radial distance - from 0 to 1 - of the shape. Saturation is not modified through the script, meaning that every color of the colorbar has maximum saturation, i.e. a radius of 1. For hue, it was decided to only take blue to red, which means that 120° of the cylinder are not used. Value ranges from 0 to 1, therefore the normalized intensity values can be directly

[3]The HSV color model is used here instead of the more widely known RGB color model, because two of the HSV color model parameters directly correspond to the lifetime and intensity parameters, thus making it easier to explain.

applied.
Thus, with one image, one can read out the lifetime value through hue and intensity through brightness (value) of each pixel. For example, two pixels with the same hue but different brightness have the same lifetime but different intensities.
To enable lifetime-intensity stacks, additional smaller steps have been added before the procedure explained above, which do not change the script's working principle but ensure that the correct lifetime values and transparency mask are applied for each frame. Figure 5.3 features a super-resolution image of neuron cells acquired in the collaboration with the Huser Group which was created by using this script.

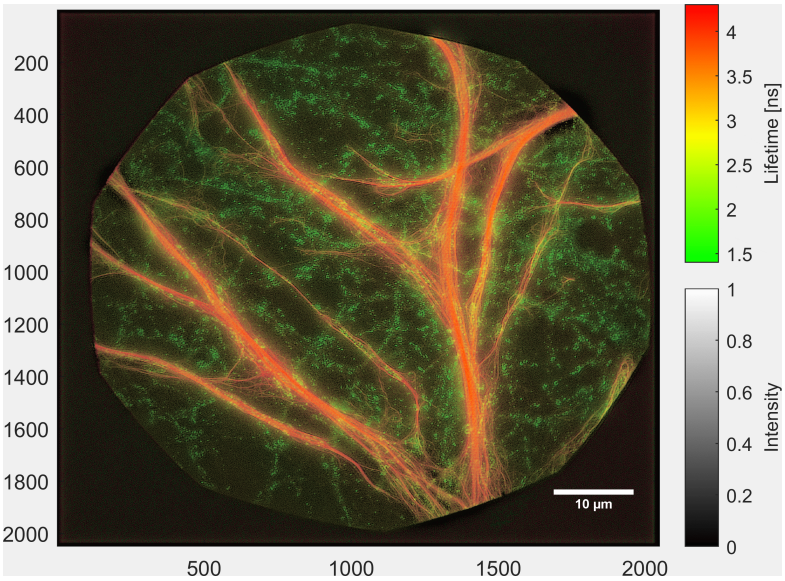

Figure 5.3: FLIM-SIM image of rat hippocampal primary neuron culture immunostained for the astrocyte marker GFAP (fluorophore: BDP-TMR) and for the mitochondrial marker TOM20 (fluorophore Cy3).

5.3 Miscellaneous scripts

More, smaller additions to scripts or new scripts have also been written for this project. Namely, a tweak to the acquisition script to work with an arbitrary number of frames. A script was created that blacks out the biggest particles and thus deletes agglomerates. A program has been written that generates an image with a random number of Gaussian signals, with programmable FWHMs, to simulate experimental data, and verifying whether the data analysis yields correct values. The LUT script has been modified to work with samples that do not match the IRF size, the reconvolution fitting script was changed to work with an arbitrary number of frames, and a script has been written to work with the SVS-VISTEK exo250ZU3 polarization camera. Additionally, a graphical user interface (GUI) has been written to combine the acquisition scripts with live imaging, including

live ratio and lifetime readout, while controlling the camera parameters to allow more straightforward navigation and management of the acquisition and live feedback of the lifetime.

5.4 Results

This section discusses the results of the data analysis improvements.

5.4.1 Overlapping Script

Tests have been run to qualitatively show the increase in accuracy of the newest versions of overlapping scripts. These tests include overlapping quadrants from super-resolution but also non-super-resolution data. The overlaps are then compared by calculating the Gaussian centroid of certain particles in both quadrants and thus inferring the shift in particle center in pixels. These shifts are compared against the shifts produced by the other overlapping versions. To conduct this, the quadrants of both methods are concatenated to a single stack. Using the Picasso software from Schnitzbauer et al. [57] a region of interest is drawn, the particles inside it localized and fitted with a least-squares 2-dimensional Gaussian. The concatenation is done to ensure the same region of interest for each quadrant. The resulting fit parameters for the Gaussian center are used to calculate the shift between quadrants by subtraction including error propagation.
Figure 5.4 shows the average shift of the ECC and TurboReg versions for the non-super-resolution data[4].

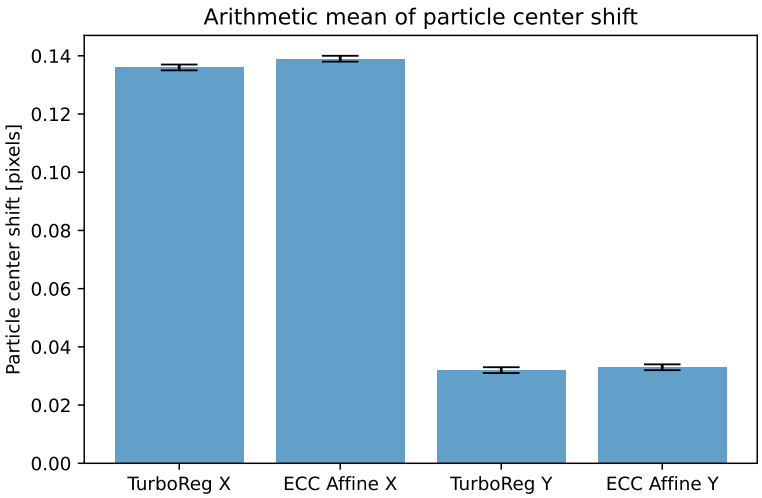

Figure 5.4: Mean values of the overlapping quality for TurboReg and the Affine Transformation of ECC for both directions.

[4]FluoSpheres™ Carboxylate-Modified Microspheres, 0.17 µm, orange fluorescent (540/560), 2% solids

TurboReg's overlap worked slightly better, both for x and y directions - (0.136 ± 0.001) pixels and (0.032 ± 0.001) pixels, respectively - against (0.139 ± 0.001) pixels and (0.033 ± 0.001) pixels for x and y. The cause for this might be the usage of an Affine Transformation for the ECC algorithm, while TurboReg constructs a 3x3 matrix for Homography giving it more degrees of freedom.
After considering this, the same particles were inspected again, but this time, the ECC algorithm used a Homography as well. The results of the ECC Homography are identical to the ones of TurboReg. The discrepancy between the centroid shifts in x and y directions is very likely due to using the top channel, where the particles are slightly elongated in x direction. To average the center shift for both directions, we take the euclidean norm. This gives us (0.140 ± 0.002) pixels for TurboReg and the ECC Homography and (0.143 ± 0.002) pixels for the ECC Affine Transformation.
Figure 5.5 compares the super-resolution data[5]. Hereby, only the Homography version of the ECC algorithm is compared against the TurboReg overlap.

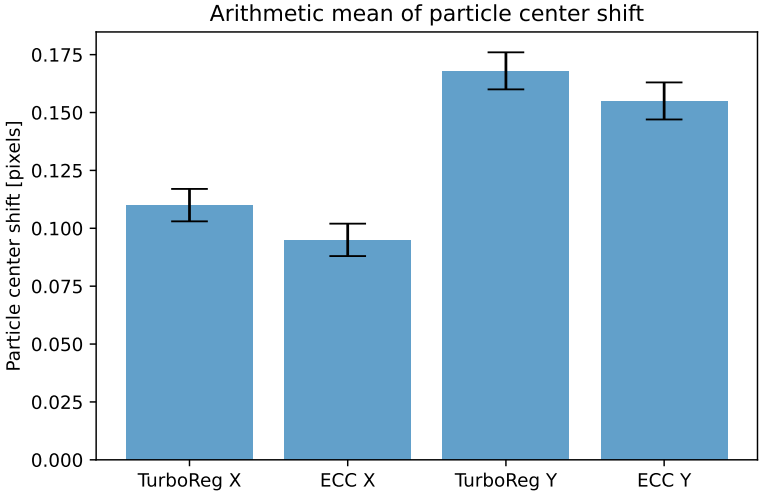

Figure 5.5: Mean values of the overlapping quality for the TurboReg and ECC algorithms for both directions for a super-resolution image.

ECC displays an overall more precise overlap with mean values of (0.095 ± 0.007) pixels and (0.155 ± 0.008) pixels for x and y directions, respectively. TurboReg is worse in y direction with (0.168 ± 0.008) pixels compared to (0.110 ± 0.007) pixels for x direction. Taking the euclidean norm gives (0.182 ± 0.008) pixels for ECC and (0.201 ± 0.008) pixels for TurboReg. The discrepancy between directions can again be due to the used channel. After both tests, one can ascertain that both overlapping methods are very precise, with ECC's homography being slightly better super-resolution images of beads. The corresponding data of both tests can be found in the appendix (7.4, 7.5, 7.6, 7.7).

[5]Mixture of FluoSpheres™ Carboxylate-Modified Microspheres, 0.17 µm, orange fluorescent (540/560), 2% solids and TetraSpeck™ Microspheres, 0.2 m, fluorescent blue/green/orange/dark red.

To determine the overlapping quality of cell samples, two FLIM-SIM cell images were used. One of them (Sample A) is visible in Figure 5.3. Again, only Homography was used for determining the transformation matrix. For a more precise overlap, a Fourier-filter was applied to both samples, thus reducing the inhomogeneities of the PC gating. The filtered samples were used as template for the unfiltered samples. After overlapping, the quadrants of both methods are again concatenated to a single stack. A line perpendicular to the string-like cell structures is drawn in ImageJ and the resulting intensity profiles are exported. The intensity profiles are fitted with a 1D Gaussian of the form:

$$f(x) = A \exp(-\frac{(x - x_0)^2}{2\sigma^2}) + b \tag{5.4}$$

The full data can be found in the appendix (7.8 and 7.9).
Sample A, the rat neurons, was slightly better overlapped by the ECC algorithm with a difference of (0.190 ± 0.094) pixels compared to TurboRegs (0.211 ± 0.092) pixels. Contrary, sample B, which is an image of COS-7 African Green Monkey fibroblasts-like cells immunostained for alpha Tubulin, is more precisely overlapped by TurboReg with (0.126 ± 0.079) pixels to ECCs (0.146 ± 0.085) pixels. Calculating the average of all super-resolution results for both algorithms leads to an average shift of (0.179 ± 0.041) pixels and (0.173 ± 0.043) pixels for TurboReg and ECC, respectively. This result is visualized in Figure 5.6.

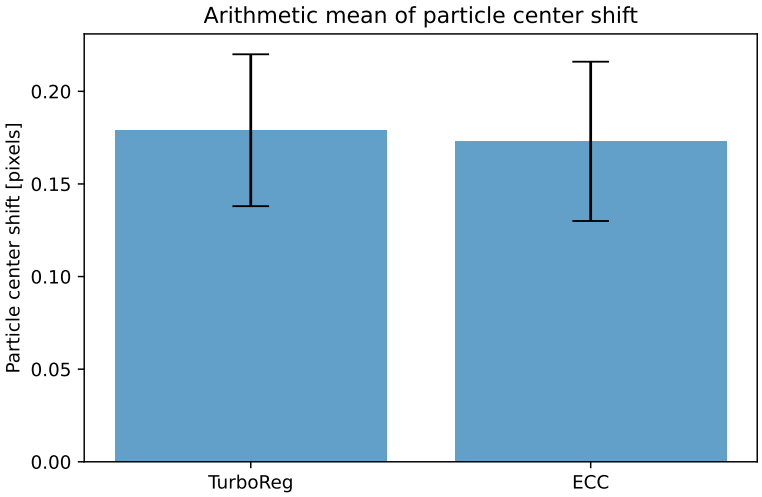

Figure 5.6: Mean values of the overlapping quality for all super-resolution data.

6 Conclusion

As stated in the result sections 4.3 and 5.4, aberrations in the physical system and inaccuracies of the data analysis could both be reduced by the performed experiments and the code written as described in this Master's thesis. The resulting resolution of the setup successfully acquired super-resolution images in collaboration with Thomas Huser's group in Bielefeld, which will be featured in an upcoming publication. The overlapping scripts then enabled further data analysis culminating in precise lifetimes, which could be displayed through the Combination script as an intensity-lifetime image or even video.
Albeit receiving satisfactory results, the setup as well as the data analysis can be further improved. For one, the setup still experiences slightly elongated PSFs due to the used polarizations. For the FLIM-SIM collaboration, this was circumvented by adding a quarter-waveplate in front of the first PSS. Furthermore, a slight defocus in one of the quadrants has been observed while inspecting images for the overlapping tests. This may come from a slight difference in path length, thus not aligning with the focal length of the achromat before the CMOS.
As for the data analysis, the tests described in section 5.4 display a displacement of overlap of (0.173 ± 0.043) pixels for the inspected super-resolution images and (0.140 ± 0.002) pixels for non-super-resolution images of beads. That the overlap is more accurate for non-super-resolution images is unexpected. A reason might be the artifacts that result from the illumination patterns used for SIM. They might be more prominent in one quadrant, hence influence the position of the ECC maximum and TurboReg minimum or the correct calculation of the Gaussian centroid. It also might be caused by the random sample used for overlap quality testing. Therefore, more extensive testing with a bigger sample size might resolve this question.
To further improve the overlap, one could implement a filter, which, for a specified intensity, filters out particles such that the algorithm has a smaller subset of points, reducing the number of outliers and noise it has to work with. Additionally, one could try to decrease the inhomogeneities present in the Pockels Cell. For the cell samples, this was done by applyig a fourier filter to the images before overlapping, which removes the low frequency inhomogeneities. This only works for the overlap of the images but does not remove the inhomogeneities of the lifetime image. Another method would be to first image a sample with beads where the overlap is satisfactory, saving the transformation matrix and then exchange the sample for one where the overlap might be unprecise. This would require the setup to be stable enough.
Decreasing the PC inhomogeneities in the resulting lifetime data is possible by calculating the lifetime for the rising as well as falling edge and then averaging them. This works because the inhomogeneities for the t_d of the rising edge and the t_d of the falling edge partially cancel each other out. The reason for this behaviour is still unknown, but it

might be due to hysteresis in the PC. If the inhomogeneities are similar over a longer duration (days), it would also be possible to calibrate them out. It is also advisable to let the PC warm up before the experiments.
Overall, improving the EOFLIM project, which was the goal of this thesis, was a success. This paves the way for future EOFLIM applications. For example, the monitoring of Cl^-, which is important for disease-relevant physiological processes, as described in [58], where acquisition time is one of the biggest limitations. Additionally, EOFLIM can be used clinically to measure NAD(P)H lifetimes [59], which are different for malignant tissue compared to healthy tissue. This allows for the quantitative assessment of cells for various types of cancers, including breast [60], oral [61], and skin [62, 63] cancers. For this procedure, the speed and sensitivity of EOFLIM might offer an advantage to the fluorescence techniques currently used. Furthermore, EOFLIM can be used in the realm of dermatology [63] to observe transdermal drug delivery or the effect cosmetic products might have on the skin. Finally, following the success of the super-resolution collaboration, the integration of EOFLIM with SR-SIM opens the possibility to extend their sample analysis to other live cells. By capturing the whole field of view at once, the peak power and therefore the degradation of these cells is reduced. Additionally, dynamic processes of these cells can now be effectively studied for a full FOV, which would not be feasible for S-R scanning FLIM techniques.

Bibliography

[1] M. Renz, "Fluorescence microscopy—a historical and technical perspective," *Cytometry Part A*, vol. 83, no. 9, pp. 767–779, 2013.

[2] D. M. Jameson, *Perspectives on Fluorescence: A Tribute to Gregorio Weber*, vol. 17. Springer, 2016.

[3] W. BECKER, "Fluorescence lifetime imaging – techniques and applications," *Journal of Microscopy*, vol. 247, no. 2, pp. 119–136, 2012.

[4] T. A. Klar and S. W. Hell, "Subdiffraction resolution in far-field fluorescence microscopy," *Opt. Lett.*, vol. 24, pp. 954–956, Jul 1999.

[5] E. Betzig, G. H. Patterson, R. Sougrat, O. W. Lindwasser, S. Olenych, J. S. Bonifacino, M. W. Davidson, J. Lippincott-Schwartz, and H. F. Hess, "Imaging intracellular fluorescent proteins at nanometer resolution," *Science*, vol. 313, pp. 1642–1645, Sept. 2006.

[6] M. Orrit, "Single molecule optics - 2011." Received: 29-6-2023.

[7] A. H. Clayton, "Frequency-domain fluorescence lifetime imaging microscopy (fd-flim)." `https://www.picoquant.com/images/uploads/page/files/17319/3_fd-flim.pdf`.

[8] T. Korte and A. Herrmann, "Fluorescence lifetime imaging microscopy by tcspc (td-flim)." `https://www.picoquant.com/images/uploads/page/files/17319/4_td_flim.pdf`.

[9] S. Orthaus-Mueller, "Rapidflim: The new and innovative method for ultra fast flim imaging." `https://www.photonics.com/White_Papers/rapidFLIM_The_New_and_Innovative_Method_for/wpp1647`. Application Note, PicoQuant.

[10] "pco.flim datasheet." `https://www.excelitas.com/de/product/pcoflim`. [Online; accessed 18-January-2024].

[11] A. J. Bowman, B. B. Klopfer, T. Juffmann, and M. A. Kasevich, "Electro-optic imaging enables efficient wide-field fluorescence lifetime microscopy," *Nature Communications*, vol. 10, p. 4561, Oct. 2019.

[12] R. Heintzmann and T. Huser, "Super-Resolution structured illumination microscopy," *Chem. Rev.*, vol. 117, pp. 13890–13908, Dec. 2017.

[13] M. T. Erkkilä, *Multimodal surgical microscope for real time neurosurgical guidance*. Phd thesis, Medical University of Vienna, 2021. Available at `https://resolver.obvsg.at/urn:nbn:at:at-ubmuw:1-46952`.

[14] M. T. Erkkilä, B. Bauer, N. Hecker-Denschlag, M. J. Madera Medina, R. A. Leitgeb, A. Unterhuber, J. Gesperger, T. Roetzer, C. Hauger, W. Drexler, and et al., "Widefield fluorescence lifetime imaging of protoporphyrin ix for fluorescence-guided neurosurgery: An ex vivo feasibility study," *Journal of Biophotonics*, vol. 12, no. 6, 2019.

[15] M. T. Erkkilä, D. Reichert, J. Gesperger, B. Kiesel, T. Roetzer, P. A. Mercea, W. Drexler, A. Unterhuber, R. A. Leitgeb, A. Woehrer, A. Rueck, M. Andreana, and G. Widhalm, "Macroscopic fluorescence-lifetime imaging of NADH and protoporphyrin IX improves the detection and grading of 5-aminolevulinic acid-stained brain tumors," *Scientific Reports*, vol. 10, p. 20492, Nov. 2020.

[16] D. Reichert, M. T. Erkkilä, G. Holst, N. Hecker-Denschlag, M. Wilzbach, C. Hauger, W. Drexler, J. Gesperger, B. Kiesel, T. Roetzer, and et al., "Towards real-time wide-field fluorescence lifetime imaging of 5-ala labeled brain tumors with multi-tap cmos cameras," *Biomedical Optics Express*, vol. 11, no. 3, p. 1598, 2020.

[17] M. T. Erkkilä, D. Reichert, N. Hecker-Denschlag, M. Wilzbach, C. Hauger, R. A. Leitgeb, J. Gesperger, B. Kiesel, T. Roetzer, G. Widhalm, and et al., "Surgical microscope with integrated fluorescence lifetime imaging for 5-aminolevulinic acid fluorescence-guided neurosurgery," *Journal of Biomedical Optics*, vol. 25, no. 07, p. 1, 2020.

[18] Wikipedia contributors, "Stokes shift diagram." `https://en.wikipedia.org/wiki/Stokes_shift#/media/File:Stokes_shift_diagram.svg`, Nov 2023. [Online; accessed 30-November-2023].

[19] R. Datta, T. M. Heaster, J. T. Sharick, A. A. Gillette, and M. C. Skala, "Fluorescence lifetime imaging microscopy: Fundamentals and advances in instrumentation, analysis, and applications," *Journal of Biomedical Optics*, vol. 25, no. 07, p. 1, 2020.

[20] *Fluorescence Microscopy*, ch. 15, pp. 383–403. John Wiley Sons, Ltd, 2019.

[21] "What is a jablonski diagram (perrin-jablonski diagram)?." `https://www.edinst.com/us/blog/jablonski-diagram-2`, Feb 2023. [Online; accessed 30-November-2023].

[22] R. Sanders, A. Draaijer, H. Gerritsen, P. Houpt, and Y. Levine, "Quantitative ph imaging in cells using confocal fluorescence lifetime imaging microscopy," *Analytical Biochemistry*, vol. 227, no. 2, pp. 302–308, 1995.

[23] C. Gota, S. Uchiyama, T. Yoshihara, S. Tobita, and T. Ohwada, "Temperature-dependent fluorescence lifetime of a fluorescent polymeric thermometer, poly(n-isopropylacrylamide), labeled by polarity and hydrogen bonding sensitive 4-sulfamoyl-

7-aminobenzofurazan," *The Journal of Physical Chemistry B*, vol. 112, no. 10, pp. 2829–2836, 2008. PMID: 18278900.

[24] D. Schweitzer, M. Hammer, F. Schweitzer, R. Anders, T. Doebbecke, S. Schenke, E. R. Gaillard, and E. R. Gaillard, "In vivo measurement of time-resolved autofluorescence at the human fundus," *Journal of Biomedical Optics*, vol. 9, no. 6, pp. 1214 – 1222, 2004.

[25] M. K. Kuimova, G. Yahioglu, J. A. Levitt, and K. Suhling, "Molecular rotor measures viscosity of live cells via fluorescence lifetime imaging," *Journal of the American Chemical Society*, vol. 130, no. 21, pp. 6672–6673, 2008. PMID: 18457396.

[26] *Optical Aberrations of the Microscope*, ch. 6, pp. 101–125. John Wiley Sons, Ltd, 2019.

[27] V. Lakshminarayanan and A. Fleck, "Zernike polynomials: A guide," *Journal of Modern Optics*, vol. 58, no. 18, p. 1678–1678, 2011.

[28] Wikipedia contributors, "Zernike airy image." `https://en.wikipedia.org/wiki/File:ZernikeAiryImage.jpg`. [Online; accessed 30-November-2023].

[29] *Diffraction and Image Formation in Microscopy*, ch. 10, pp. 211–242. John Wiley Sons, Ltd, 2019.

[30] *Polarised-Light Microscopy: Part 1 – Theory*, ch. 13, pp. 317–346. John Wiley Sons, Ltd, 2019.

[31] S. Konijnenberg, A. J. Adam, and H. P. Urbach, *BSc Optics*. TU Delft Open, 2021.

[32] K. K. Sharma, *Optics : principles and applications*. Amsterdam ; Boston :: Academic Press,, 1st edition ed., 2006.

[33] Wikipedia contributors, "File:poincare-sphere stokes.svg." `https://commons.wikimedia.org/w/index.php?title=File:Poincare-sphere_stokes.svg&oldid=808543937`, 2023. [Online; accessed 1-December-2023].

[34] R. Hartley and A. Zisserman, *Multiple View Geometry in Computer Vision*. New York, NY, USA: Cambridge University Press, 2 ed., 2003.

[35] D. Lenton, "Part ii: Projective transformations in 2d." `https://medium.com/@unifyai/part-ii-projective-transformations-in-2d-2e99ac9c7e9f#:~:text=The%20important%20point%20to%20note,degrees%20of%20freedom%2C%20not%20nine`, Jun 2019. [Online; accessed 15-January-2024].

[36] baeldung, "Differences between homography and affine transformation." `https://www.baeldung.com/cs/homography-vs-affine-transformation`, Jun 2023. [Online; accessed 15-January-2024].

[37] A. J. Bowman and M. A. Kasevich, "Electro-optic imaging: combining space and time in free-space optics," *Optical Society of America*, 2020.

[38] A. Weidlich and A. Wilkie, "Realistic rendering of birefringency in uniaxial crystals," *ACM Trans. Graph.*, vol. 27, mar 2008.

[39] V. Morozov, A. Olenin, V. Tunkin, D. Yakovlev, V. Rusov, A. Gorchakov, and S. Doroganov, "Picosecond pulsed-periodic high-peak power nd:yag laser operationally controlled by ktp-based pockels cell," *Crystals*, vol. 12, no. 3, 2022.

[40] "Whitepaper: What's the best way to modulate my laser beam – aom or eom?." `https://gandh.com/news-and-resources/what-s-the-best-way-to-modulate-my-laser-beam-aom-or-eom`. [Online; accessed 30-November-2023].

[41] "Shack-hartmann wavefront sensors." `https://www.thorlabs.com/newgrouppage9.cfm?objectgroup_id=5287`. [Online; accessed 30-November-2023].

[42] Wikipedia contributors, "Schematic of a fluorescence microscope." `https://en.wikipedia.org/wiki/Fluorescence_microscope#/media/File:FluorescenceFilters_2008-09-28.svg`, 2023. [Online; accessed 30-November-2023].

[43] M. Y. Berezin and S. Achilefu, "Fluorescence lifetime measurements and biological imaging," *Chemical Reviews*, vol. 110, no. 5, pp. 2641–2684, 2010. PMID: 20356094.

[44] G. S. Bumbrah and R. M. Sharma, "Raman spectroscopy – basic principle, instrumentation and selected applications for the characterization of drugs of abuse," *Egyptian Journal of Forensic Sciences*, vol. 6, no. 3, pp. 209–215, 2016.

[45] D. Bovenkamp, A. Micko, J. Püls, F. Placzek, R. Höftberger, G. Vila, R. Leitgeb, W. Drexler, M. Andreana, S. Wolfsberger, and A. Unterhuber, "Line scan raman microspectroscopy for label-free diagnosis of human pituitary biopsies," *Molecules*, vol. 24, p. 3577, Oct. 2019.

[46] L. Wong Kee Song, D. Adler, J. Conway, D. Diehl, F. Farraye, S. Kantsevoy, R. Kwon, P. Mamula, B. Rodriguez, R. Shah, and W. Tierney, "Narrow band imaging and multiband imaging," *Gastrointestinal endoscopy*, vol. 67, pp. 581–589, Apr. 2008.

[47] Y. Soda, C. Myskiw, A. Rommel, and I. M. Verma, "Mechanisms of neovascularization and resistance to anti-angiogenic therapies in glioblastoma multiforme," *Journal of Molecular Medicine*, vol. 91, p. 439–448, Mar. 2013.

[48] Andor, "Structured illumination microscopy and 3d sim imaging." `https://andor.oxinst.com/learning/view/article/super-resolution-imaging-structured-illumination-microscopy`. Accessed: 30.11.2023.

[49] A. C. Descloux, K. S. Grußmayer, V. Navikas, D. Mahecic, S. Manley, and A. Radenovic, "Experimental combination of Super-Resolution optical fluctuation imaging with structured illumination microscopy for large Fields-of-View," *ACS Photonics*, vol. 8, pp. 2440–2449, Aug. 2021.

[50] M. G. L. Gustafsson, "Nonlinear structured-illumination microscopy: Wide-field fluorescence imaging with theoretically unlimited resolution," *Proceedings of the National Academy of Sciences*, vol. 102, no. 37, pp. 13081–13086, 2005.

[51] G. T. Dempsey, "Chapter 24 - a user's guide to localization-based super-resolution fluorescence imaging," in *Digital Microscopy* (G. Sluder and D. E. Wolf, eds.), vol. 114 of *Methods in Cell Biology*, pp. 561–592, Academic Press, 2013.

[52] R. Marchand, F. I. Pfanner, D. Aziz, N. Jarnot, and T. Juffmann, "Fast, sensitive and versatile electro-optic fluorescence lifetime imaging microscopy," in *Biophotonics Congress: Optics in the Life Sciences 2023 (OMA, NTM, BODA, OMP, BRAIN)*, p. NTu2C.4, Optica Publishing Group, 2023.

[53] G. D. Evangelidis and E. Z. Psarakis, "Parametric image alignment using enhanced correlation coefficient maximization," *IEEE Transactions on Pattern Analysis and Machine Intelligence*, vol. 30, no. 10, pp. 1858–1865, 2008.

[54] H. P. Gavin, "The levenberg-marquardt method for nonlinear least squares curve-fitting problems," 2013.

[55] P. Thevenaz, U. Ruttimann, and M. Unser, "A pyramid approach to subpixel registration based on intensity," *IEEE Transactions on Image Processing*, vol. 7, pp. 27–41, January 1998.

[56] C. Ding, J. Gu, X. Ma, F. Gao, and Y. Li, "Target recognition in different color spaces," pp. 151–155, 08 2013.

[57] J. Schnitzbauer, M. T. Strauss, T. Schlichthaerle, F. Schueder, and R. Jungmann, "Super-resolution microscopy with dna-paint," *Nature Protocols*, vol. 12, pp. 1198–1228, Jun 2017.

[58] T. Gensch, V. Untiet, A. Franzen, P. Kovermann, and C. Fahlke, *Determination of Intracellular Chloride Concentrations by Fluorescence Lifetime Imaging*, pp. 189–211. Cham: Springer International Publishing, 2015.

[59] A. J. Walsh, A. T. Shah, J. T. Sharick, and M. C. Skala, *Fluorescence Lifetime Measurements of NAD(P)H in Live Cells and Tissue*, pp. 435–456. Cham: Springer International Publishing, 2015.

[60] D. K. Bird, L. Yan, K. M. Vrotsos, K. W. Eliceiri, E. M. Vaughan, P. J. Keely, J. G. White, and N. Ramanujam, "Metabolic mapping of MCF10A human breast cells via multiphoton fluorescence lifetime imaging of the coenzyme NADH," *Cancer Res.*, vol. 65, pp. 8766–8773, Oct. 2005.

[61] A. T. Shah, M. Demory Beckler, A. J. Walsh, W. P. Jones, P. R. Pohlmann, and M. C. Skala, "Optical metabolic imaging of treatment response in human head and neck squamous cell carcinoma," *PLoS One*, vol. 9, p. e90746, Mar. 2014.

[62] N. P. Galletly, J. McGinty, C. Dunsby, F. Teixeira, J. Requejo-Isidro, I. Munro, D. S. Elson, M. A. A. Neil, A. C. Chu, P. M. W. French, and G. W. Stamp, "Fluorescence lifetime imaging distinguishes basal cell carcinoma from surrounding uninvolved skin," *Br. J. Dermatol.*, vol. 159, pp. 152–161, July 2008.

[63] W. Y. Sanchez, M. Pastore, I. N. Haridass, K. König, W. Becker, and M. S. Roberts, *Fluorescence Lifetime Imaging of the Skin*, pp. 457–508. Cham: Springer International Publishing, 2015.

7 Appendix

	BS1 ± 0.001	BS2 ± 0.001	BS3 ± 0.001	BS4 ± 0.001
Trans 1	-0.002	-0.016	0	0.002
Refl 1	-0.014	-0.011	-0.017	-0.017
Trans 2	-0.001	-0.015	0.001	0
Refl 2	-0.013	-0.011	-0.015	-0.014

Table 7.1: Coefficients for Zernike Polynomial c_4. Errors (± 0.001) are the visible fluctuation of the wavefront-sensor data.

	BS1 ± 0.001	BS2 ± 0.001	BS3 ± 0.001	BS4 ± 0.001
Trans 1	-0.003	0.013	-0.006	-0.003
Refl 1	0.017	0.016	0.016	0.019
Trans 2	-0.002	0.012	-0.006	-0.003
Refl 2	0.016	0.018	0.01	0.018

Table 7.2: Coefficients for Zernike Polynomial c_6. Errors (± 0.001) are the visible fluctuation of the wavefront-sensor data.

Multiprocessing (s)	Multithreading (s)	Standard (s)
228.55	209.87	218.73
226.60	207.49	214.10
223.31	212.37	217.36
224.14	212.46	212.53
223.21	208.41	221.28
$\bar{x} = 225.16$	$\bar{x} = 210.12$	$\bar{x} = 214.8$

Table 7.3: Comparison between 3 different modes of the same script.

Particle	TurboReg X-Direction (Pixels)	TurboReg Y-Direction (Pixels)	ECC Affine X-Direction (Pixels)	ECC AffineY-Direction (Pixels)
1	0.006 ± 0.006	0.015 ± 0.005	0.025 ± 0.006	0.014 ± 0.005
2	0.325 ± 0.006	0.115 ± 0.004	0.294 ± 0.006	0.115 ± 0.004
3	0.226 ± 0.006	0.109 ± 0.005	0.202 ± 0.006	0.113 ± 0.005
4	0.017 ± 0.006	0.059 ± 0.004	0.025 ± 0.006	0.061 ± 0.004
5	0.069 ± 0.006	0.056 ± 0.004	0.037 ± 0.006	0.056 ± 0.004
6	0.092 ± 0.008	0.033 ± 0.005	0.102 ± 0.008	0.035 ± 0.005
7	0.032 ± 0.006	0.061 ± 0.004	0.062 ± 0.006	0.060 ± 0.004
8	0.039 ± 0.006	0.037 ± 0.004	0.037 ± 0.006	0.038 ± 0.004
9	0.070 ± 0.005	0.006 ± 0.004	0.093 ± 0.006	0.003 ± 0.004
10	0.128 ± 0.006	0.004 ± 0.004	0.132 ± 0.006	0.006 ± 0.004
11	0.436 ± 0.008	0.031 ± 0.006	0.433 ± 0.009	0.028 ± 0.006
12	0.266 ± 0.007	0.050 ± 0.005	0.269 ± 0.007	0.030 ± 0.005
13	0.175 ± 0.006	0.007 ± 0.004	0.176 ± 0.006	0.023 ± 0.004
14	0.169 ± 0.006	0.000 ± 0.004	0.169 ± 0.006	0.000 ± 0.004
15	0.173 ± 0.005	0.100 ± 0.005	0.160 ± 0.005	0.125 ± 0.005
16	0.174 ± 0.007	0.046 ± 0.005	0.165 ± 0.007	0.048 ± 0.005
17	0.100 ± 0.006	0.049 ± 0.004	0.112 ± 0.006	0.058 ± 0.004
18	0.191 ± 0.006	0.006 ± 0.004	0.185 ± 0.006	0.005 ± 0.004
19	0.237 ± 0.009	0.003 ± 0.006	0.237 ± 0.010	0.003 ± 0.006
20	0.214 ± 0.006	0.043 ± 0.004	0.182 ± 0.006	0.043 ± 0.004
21	0.135 ± 0.004	0.014 ± 0.003	0.103 ± 0.004	0.013 ± 0.003
22	0.220 ± 0.007	0.040 ± 0.005	0.190 ± 0.007	0.040 ± 0.005
23	0.214 ± 0.005	0.072 ± 0.003	0.190 ± 0.005	0.069 ± 0.003
24	0.124 ± 0.006	0.015 ± 0.004	0.124 ± 0.006	0.015 ± 0.004
25	0.139 ± 0.007	0.025 ± 0.004	0.105 ± 0.007	0.020 ± 0.004
26	0.175 ± 0.006	0.009 ± 0.004	0.169 ± 0.006	0.012 ± 0.004
27	0.082 ± 0.008	0.023 ± 0.005	0.046 ± 0.009	0.017 ± 0.005
28	0.127 ± 0.009	0.045 ± 0.006	0.095 ± 0.009	0.045 ± 0.006
29	0.132 ± 0.007	0.021 ± 0.004	0.109 ± 0.007	0.018 ± 0.005
30	0.141 ± 0.007	0.030 ± 0.005	0.120 ± 0.007	0.023 ± 0.005
31	0.219 ± 0.006	0.032 ± 0.004	0.190 ± 0.006	0.031 ± 0.004
32	0.195 ± 0.008	0.083 ± 0.005	0.164 ± 0.008	0.083 ± 0.005
33	0.062 ± 0.007	0.022 ± 0.005	0.030 ± 0.007	0.022 ± 0.005
34	0.021 ± 0.008	0.104 ± 0.005	0.010 ± 0.009	0.104 ± 0.005
35	0.083 ± 0.007	0.024 ± 0.005	0.052 ± 0.007	0.024 ± 0.005
36	0.050 ± 0.008	0.103 ± 0.006	0.027 ± 0.009	0.087 ± 0.006
37	0.037 ± 0.008	0.038 ± 0.005	0.069 ± 0.008	0.038 ± 0.005
38	0.042 ± 0.007	0.055 ± 0.004	0.012 ± 0.007	0.054 ± 0.004
39	0.031 ± 0.007	0.029 ± 0.005	0.060 ± 0.007	0.029 ± 0.005
40	0.092 ± 0.006	0.007 ± 0.004	0.126 ± 0.006	0.032 ± 0.005
41	0.064 ± 0.006	0.014 ± 0.005	0.090 ± 0.007	0.028 ± 0.005
42	0.089 ± 0.006	0.035 ± 0.004	0.122 ± 0.006	0.037 ± 0.004
$\bar{x}$	0.136 ± 0.001	0.032 ± 0.001	0.139 ± 0.001	0.033 ± 0.001

Table 7.4: Particle center shifts for the non-super-resolution particles. TurboReg and ECC Affine transformation.

Particle	ECC Homography X-Direction (Pixels)	ECC Homography Y-Direction (Pixels)
1	0.006 ± 0.006	0.015 ± 0.005
2	0.325 ± 0.006	0.115 ± 0.004
3	0.226 ± 0.006	0.109 ± 0.005
4	0.017 ± 0.006	0.059 ± 0.004
5	0.069 ± 0.006	0.056 ± 0.004
6	0.092 ± 0.008	0.033 ± 0.005
7	0.032 ± 0.006	0.061 ± 0.004
8	0.039 ± 0.006	0.037 ± 0.004
9	0.070 ± 0.005	0.006 ± 0.004
10	0.128 ± 0.006	0.004 ± 0.004
11	0.436 ± 0.008	0.031 ± 0.006
12	0.266 ± 0.007	0.050 ± 0.005
13	0.175 ± 0.006	0.007 ± 0.004
14	0.169 ± 0.006	0.000 ± 0.004
15	0.173 ± 0.005	0.100 ± 0.005
16	0.174 ± 0.007	0.046 ± 0.005
17	0.100 ± 0.006	0.049 ± 0.004
18	0.191 ± 0.006	0.006 ± 0.004
19	0.237 ± 0.009	0.003 ± 0.006
20	0.214 ± 0.006	0.043 ± 0.004
21	0.135 ± 0.004	0.014 ± 0.003
22	0.220 ± 0.007	0.040 ± 0.005
23	0.214 ± 0.005	0.072 ± 0.003
24	0.124 ± 0.006	0.015 ± 0.004
25	0.139 ± 0.007	0.025 ± 0.004
26	0.175 ± 0.006	0.009 ± 0.004
27	0.082 ± 0.008	0.023 ± 0.005
28	0.127 ± 0.009	0.045 ± 0.006
29	0.132 ± 0.007	0.021 ± 0.004
30	0.141 ± 0.007	0.030 ± 0.005
31	0.219 ± 0.006	0.032 ± 0.004
32	0.195 ± 0.008	0.083 ± 0.005
33	0.062 ± 0.007	0.022 ± 0.005
34	0.021 ± 0.008	0.104 ± 0.005
35	0.083 ± 0.007	0.024 ± 0.005
36	0.050 ± 0.008	0.103 ± 0.006
37	0.037 ± 0.008	0.038 ± 0.005
38	0.042 ± 0.007	0.055 ± 0.004
39	0.031 ± 0.007	0.029 ± 0.005
40	0.092 ± 0.006	0.007 ± 0.004
41	0.064 ± 0.006	0.014 ± 0.005
42	0.089 ± 0.006	0.035 ± 0.004
$\bar{x}$	0.136 ± 0.001	0.032 ± 0.001

Table 7.5: Particle center shifts for the non-super-resolution particles. ECC Homography transformation.

Particle	TurboReg X-Direction(Pixels)	TurboReg Y-Direction (Pixels)	ECC Homography X-Direction	ECC Homography Y-Direction
1	0.098 ± 0.042	0.207 ± 0.043	0.065 ± 0.042	0.149 ± 0.043
2	0.019 ± 0.063	0.022 ± 0.070	0.070 ± 0.057	0.089 ± 0.063
3	0.005 ± 0.063	0.098 ± 0.074	0.041 ± 0.063	0.191 ± 0.073
4	0.098 ± 0.047	0.123 ± 0.052	0.095 ± 0.047	0.055 ± 0.052
5	0.156 ± 0.052	0.254 ± 0.058	0.155 ± 0.052	0.147 ± 0.058
6	0.153 ± 0.052	0.110 ± 0.062	0.152 ± 0.052	0.017 ± 0.062
7	0.147 ± 0.056	0.262 ± 0.067	0.104 ± 0.056	0.354 ± 0.067
8	0.191 ± 0.057	0.352 ± 0.076	0.141 ± 0.057	0.409 ± 0.075
9	0.113 ± 0.058	0.157 ± 0.071	0.074 ± 0.058	0.264 ± 0.071
10	0.152 ± 0.067	0.135 ± 0.075	0.095 ± 0.067	0.199 ± 0.075
11	0.183 ± 0.058	0.062 ± 0.089	0.125 ± 0.058	0.133 ± 0.089
12	0.137 ± 0.052	0.184 ± 0.072	0.072 ± 0.052	0.082 ± 0.072
13	0.132 ± 0.055	0.117 ± 0.071	0.065 ± 0.055	0.028 ± 0.071
14	0.096 ± 0.060	0.086 ± 0.078	0.032 ± 0.060	0.143 ± 0.077
15	0.369 ± 0.068	0.177 ± 0.078	0.335 ± 0.069	0.238 ± 0.078
16	0.042 ± 0.057	0.245 ± 0.073	0.014 ± 0.058	0.151 ± 0.073
17	0.278 ± 0.060	0.106 ± 0.075	0.211 ± 0.060	0.050 ± 0.075
18	0.165 ± 0.056	0.353 ± 0.084	0.125 ± 0.056	0.446 ± 0.083
19	0.070 ± 0.055	0.331 ± 0.076	0.008 ± 0.055	0.250 ± 0.076
20	0.223 ± 0.061	0.472 ± 0.087	0.183 ± 0.062	0.406 ± 0.088
21	0.228 ± 0.057	0.024 ± 0.084	0.169 ± 0.058	0.087 ± 0.085
22	0.002 ± 0.056	0.060 ± 0.077	0.034 ± 0.056	0.031 ± 0.078
23	0.204 ± 0.059	0.068 ± 0.074	0.175 ± 0.059	0.128 ± 0.074
24	0.027 ± 0.057	0.194 ± 0.087	0.021 ± 0.058	0.116 ± 0.087
25	0.125 ± 0.059	0.220 ± 0.069	0.065 ± 0.059	0.306 ± 0.069
26	0.219 ± 0.065	0.129 ± 0.066	0.156 ± 0.065	0.078 ± 0.066
27	0.098 ± 0.057	0.185 ± 0.087	0.062 ± 0.057	0.096 ± 0.087
28	0.038 ± 0.069	0.169 ± 0.088	0.000 ± 0.069	0.246 ± 0.088
29	0.012 ± 0.057	0.056 ± 0.071	0.055 ± 0.057	0.030 ± 0.071
30	0.240 ± 0.059	0.374 ± 0.063	0.206 ± 0.059	0.293 ± 0.063
31	0.027 ± 0.057	0.013 ± 0.083	0.117 ± 0.058	0.045 ± 0.084
32	0.046 ± 0.067	0.036 ± 0.071	0.087 ± 0.067	0.106 ± 0.071
33	0.111 ± 0.055	0.377 ± 0.056	0.050 ± 0.055	0.295 ± 0.056
34	0.097 ± 0.052	0.219 ± 0.058	0.043 ± 0.052	0.131 ± 0.058
35	0.051 ± 0.056	0.159 ± 0.061	0.014 ± 0.056	0.058 ± 0.061
36	0.132 ± 0.053	0.416 ± 0.073	0.202 ± 0.054	0.336 ± 0.074
37	0.000 ± 0.054	0.061 ± 0.063	0.056 ± 0.054	0.005 ± 0.062
38	0.020 ± 0.055	0.505 ± 0.083	0.083 ± 0.055	0.572 ± 0.083
39	0.169 ± 0.056	0.285 ± 0.073	0.226 ± 0.056	0.227 ± 0.074
40	0.026 ± 0.057	0.065 ± 0.073	0.054 ± 0.057	0.014 ± 0.073
41	0.053 ± 0.055	0.168 ± 0.087	0.000 ± 0.055	0.092 ± 0.087
42	0.129 ± 0.076	0.004 ± 0.075	0.067 ± 0.076	0.084 ± 0.075
43	0.041 ± 0.069	0.252 ± 0.076	0.024 ± 0.069	0.309 ± 0.076
44	0.067 ± 0.055	0.130 ± 0.079	0.125 ± 0.056	0.056 ± 0.078
45	0.010 ± 0.053	0.018 ± 0.059	0.034 ± 0.054	0.074 ± 0.059

Table 7.6: Particle center shifts for the super-resolution data. Part 1

Particle	TurboReg X-Direction(Pixels)	TurboReg Y-Direction (Pixels)	ECC Homography X-Direction	ECC Homography Y-Direction
46	0.000 ± 0.068	0.190 ± 0.077	0.040 ± 0.068	0.283 ± 0.076
47	0.024 ± 0.064	0.140 ± 0.071	0.017 ± 0.065	0.072 ± 0.071
48	0.034 ± 0.060	0.025 ± 0.076	0.079 ± 0.060	0.035 ± 0.076
49	0.115 ± 0.053	0.308 ± 0.073	0.148 ± 0.053	0.237 ± 0.073
50	0.089 ± 0.052	0.213 ± 0.053	0.025 ± 0.052	0.153 ± 0.053
51	0.059 ± 0.064	0.099 ± 0.060	0.127 ± 0.064	0.163 ± 0.060
52	0.141 ± 0.054	0.188 ± 0.062	0.107 ± 0.054	0.122 ± 0.062
53	0.235 ± 0.072	0.001 ± 0.061	0.177 ± 0.071	0.068 ± 0.061
54	0.067 ± 0.047	0.215 ± 0.053	0.000 ± 0.047	0.163 ± 0.053
55	0.050 ± 0.047	0.201 ± 0.053	0.008 ± 0.047	0.133 ± 0.053
56	0.044 ± 0.058	0.047 ± 0.060	0.006 ± 0.058	0.108 ± 0.060
57	0.089 ± 0.062	0.090 ± 0.062	0.134 ± 0.062	0.158 ± 0.062
58	0.078 ± 0.061	0.048 ± 0.077	0.025 ± 0.061	0.012 ± 0.077
59	0.188 ± 0.070	0.038 ± 0.065	0.137 ± 0.068	0.045 ± 0.065
60	0.411 ± 0.055	0.098 ± 0.066	0.353 ± 0.055	0.037 ± 0.066
61	0.305 ± 0.056	0.222 ± 0.064	0.257 ± 0.056	0.152 ± 0.064
62	0.317 ± 0.065	0.269 ± 0.069	0.260 ± 0.065	0.218 ± 0.069
63	0.039 ± 0.056	0.070 ± 0.064	0.092 ± 0.056	0.012 ± 0.063
64	0.046 ± 0.056	0.208 ± 0.068	0.092 ± 0.055	0.138 ± 0.067
65	0.007 ± 0.069	0.519 ± 0.103	0.057 ± 0.070	0.475 ± 0.103
66	0.169 ± 0.068	0.304 ± 0.075	0.119 ± 0.069	0.358 ± 0.075
67	0.241 ± 0.067	0.330 ± 0.084	0.187 ± 0.067	0.280 ± 0.083
68	0.076 ± 0.070	0.095 ± 0.065	0.005 ± 0.071	0.033 ± 0.065
69	0.011 ± 0.051	0.265 ± 0.055	0.075 ± 0.052	0.209 ± 0.055
70	0.167 ± 0.059	0.199 ± 0.073	0.098 ± 0.062	0.247 ± 0.075
71	0.021 ± 0.067	0.005 ± 0.074	0.087 ± 0.068	0.066 ± 0.075
72	0.052 ± 0.064	0.081 ± 0.063	0.001 ± 0.064	0.024 ± 0.063
73	0.175 ± 0.065	0.077 ± 0.081	0.133 ± 0.065	0.027 ± 0.080
74	0.007 ± 0.056	0.301 ± 0.057	0.040 ± 0.056	0.234 ± 0.057
75	0.443 ± 0.071	0.387 ± 0.063	0.389 ± 0.065	0.328 ± 0.060
76	0.154 ± 0.064	0.207 ± 0.069	0.088 ± 0.064	0.125 ± 0.068
77	0.105 ± 0.060	0.211 ± 0.066	0.043 ± 0.060	0.149 ± 0.066
78	0.087 ± 0.067	0.050 ± 0.080	0.119 ± 0.069	0.011 ± 0.083
79	0.111 ± 0.059	0.011 ± 0.061	0.168 ± 0.059	0.054 ± 0.061
80	0.038 ± 0.082	0.008 ± 0.087	0.006 ± 0.082	0.084 ± 0.087
81	0.023 ± 0.059	0.077 ± 0.068	0.026 ± 0.059	0.018 ± 0.068
82	0.112 ± 0.062	0.239 ± 0.071	0.061 ± 0.063	0.152 ± 0.070
83	0.115 ± 0.068	0.177 ± 0.072	0.068 ± 0.067	0.114 ± 0.070
84	0.015 ± 0.063	0.052 ± 0.072	0.044 ± 0.063	0.130 ± 0.071
85	0.131 ± 0.060	0.416 ± 0.062	0.067 ± 0.060	0.354 ± 0.062
86	0.017 ± 0.063	0.096 ± 0.078	0.059 ± 0.063	0.144 ± 0.077
87	0.015 ± 0.055	0.043 ± 0.056	0.081 ± 0.055	0.028 ± 0.056
88	0.118 ± 0.063	0.032 ± 0.070	0.054 ± 0.064	0.099 ± 0.070
89	0.057 ± 0.053	0.052 ± 0.057	0.004 ± 0.053	0.113 ± 0.058
$\bar{x}$	0.110 ± 0.007	0.168 ± 0.008	0.095 ± 0.007	0.155 ± 0.008

Table 7.7: Particle center shifts for the super-resolution data. Part 2

Cell	TurboReg (Pixels)	ECC (Pixels)
1	0.439 ± 0.222	0.421 ± 0.226
2	0.198 ± 0.125	0.117 ± 0.130
3	0.027 ± 0.104	0.031 ± 0.104
$\bar{x}$	0.211 ± 0.092	0.190 ± 0.094

Table 7.8: Gaussian center shifts for the rat neurons.

Cell	TurboReg (Pixels)	ECC (Pixels)
1	0.08 ± 0.113	0.031 ± 0.144
2	0.092 ± 0.155	0.146 ± 0.158
3	0.205 ± 0.138	0.260 ± 0.136
$\bar{x}$	0.126 ± 0.079	0.146 ± 0.085

Table 7.9: Gaussian center shifts for COS-7 African Green Monkey fibroblasts-like cells immunostained for alpha Tubulin

Ratio	Lifetime (ns)	Ratio	Lifetime (ns)	Ratio	Lifetime (ns)	Ratio	Lifetime (ns)	Ratio	Lifetime (ns)
0.169	20,5	0.219	13,95112	0.269	10,69679	0.319	8,561108	0.369	7,031935
0.170	20,34672	0.220	13,86975	0.270	10,64505	0.320	8,524278	0.370	7,004431
0.171	20,12117	0.221	13,78839	0.271	10,59331	0.321	8,488564	0.371	6,979261
0.172	19,90458	0.222	13,70702	0.272	10,54156	0.322	8,455009	0.372	6,95454
0.173	19,6984	0.223	13,62566	0.273	10,49061	0.323	8,421453	0.373	6,929818
0.174	19,49286	0.224	13,5443	0.274	10,44289	0.324	8,387898	0.374	6,905096
0.175	19,30382	0.225	13,46555	0.275	10,39517	0.325	8,354343	0.375	6,880374
0.176	19,11478	0.226	13,38992	0.276	10,34745	0.326	8,320788	0.376	6,855652
0.177	18,93174	0.227	13,31429	0.277	10,29973	0.327	8,287233	0.377	6,83093
0.178	18,75795	0.228	13,23867	0.278	10,252	0.328	8,253678	0.378	6,806209
0.179	18,58417	0.229	13,16304	0.279	10,20428	0.329	8,220122	0.379	6,781487
0.180	18,41743	0.230	13,08742	0.280	10,15656	0.330	8,186567	0.380	6,756765
0.181	18,2573	0.231	13,01179	0.281	10,10884	0.331	8,153012	0.381	6,732043
0.182	18,09718	0.232	12,9407	0.282	10,06112	0.332	8,119457	0.382	6,707321
0.183	17,94188	0.233	12,87044	0.283	10,0134	0.333	8,085902	0.383	6,6826
0.184	17,79404	0.234	12,80019	0.284	9,968421	0.334	8,052347	0.384	6,657877
0.185	17,64621	0.235	12,72993	0.285	9,924518	0.335	8,018792	0.385	6,633156
0.186	17,49849	0.236	12,65967	0.286	9,880613	0.336	7,986604	0.386	6,608434
0.187	17,36176	0.237	12,58942	0.287	9,836709	0.337	7,956157	0.387	6,583712
0.188	17,22503	0.238	12,51916	0.288	9,792805	0.338	7,925709	0.388	6,55899
0.189	17,0883	0.239	12,45257	0.289	9,7489	0.339	7,895262	0.389	6,534268
0.190	16,95514	0.240	12,38736	0.290	9,704997	0.340	7,864814	0.390	6,509547
0.191	16,8285	0.241	12,32215	0.291	9,661093	0.341	7,834367	0.391	6,486433
0.192	16,70186	0.242	12,25693	0.292	9,617188	0.342	7,803919	0.392	6,464332
0.193	16,57521	0.243	12,19172	0.293	9,573284	0.343	7,773471	0.393	6,44223
0.194	16,4523	0.244	12,1265	0.294	9,52938	0.344	7,743024	0.394	6,420129
0.195	16,33486	0.245	12,06129	0.295	9,486676	0.345	7,712576	0.395	6,398027
0.196	16,21742	0.246	11,99636	0.296	9,446399	0.346	7,682129	0.396	6,375926
0.197	16,09997	0.247	11,9359	0.297	9,406122	0.347	7,651681	0.397	6,353825
0.198	15,98378	0.248	11,87543	0.298	9,365845	0.348	7,621234	0.398	6,331723
0.199	15,87476	0.249	11,81496	0.299	9,325568	0.349	7,590786	0.399	6,309621
0.200	15,76574	0.250	11,7545	0.300	9,285292	0.350	7,560339	0.400	6,28752
0.201	15,65672	0.251	11,69403	0.301	9,245014	0.351	7,529891	0.401	6,265419
0.202	15,54769	0.252	11,63357	0.302	9,204738	0.352	7,499498	0.402	6,243317
0.203	15,44303	0.253	11,5731	0.303	9,16446	0.353	7,471994	0.403	6,221216
0.204	15,34175	0.254	11,51263	0.304	9,124184	0.354	7,44449	0.404	6,199114
0.205	15,24047	0.255	11,45571	0.305	9,083906	0.355	7,416986	0.405	6,177012
0.206	15,13919	0.256	11,39973	0.306	9,04363	0.356	7,389483	0.406	6,154911
0.207	15,03791	0.257	11,34375	0.307	9,003352	0.357	7,361979	0.407	6,13281
0.208	14,9411	0.258	11,28776	0.308	8,966236	0.358	7,334476	0.408	6,110708
0.209	14,84697	0.259	11,23178	0.309	8,929406	0.359	7,306972	0.409	6,088607
0.210	14,75284	0.260	11,17579	0.310	8,892576	0.360	7,279468	0.410	6,066505
0.211	14,6587	0.261	11,11981	0.311	8,855746	0.361	7,251965	0.411	6,044404
0.212	14,56457	0.262	11,06382	0.312	8,818916	0.362	7,224461	0.412	6,022302
0.213	14,47252	0.263	11,00784	0.313	8,782086	0.363	7,196957	0.413	6,000201
0.214	14,385	0.264	10,9555	0.314	8,745256	0.364	7,169454	0.414	5,980536
0.215	14,29748	0.265	10,90376	0.315	8,708426	0.365	7,14195	0.415	5,960892
0.216	14,20997	0.266	10,85202	0.316	8,671597	0.366	7,114446	0.416	5,941249
0.217	14,12245	0.267	10,80028	0.317	8,634768	0.367	7,086943	0.417	5,921606
0.218	14,03494	0.268	10,74853	0.318	8,597938	0.368	7,059439	0.418	5,901963

Table 7.10: Partial LUT for the center pixel of an image. The ratio (left) is varied from 0 to 1 in increments of 0.01 instead of the lifetime (right).